A mechanically strong and ductile soft magnet with extremely low coercivity

Liuliu Han[1], Fernando Maccari[2], Isnaldi R. Souza Filho[1], Nicolas J. Peter[1], Ye Wei[1], Baptiste Gault[1], Oliver Gutfleisch[2], Zhiming Li[3✉] & Dierk Raabe[1✉]

Soft magnetic materials (SMMs) serve in electrical applications and sustainable energy supply, allowing magnetic flux variation in response to changes in applied magnetic field, at low energy loss[1]. The electrification of transport, households and manufacturing leads to an increase in energy consumption owing to hysteresis losses[2]. Therefore, minimizing coercivity, which scales these losses, is crucial[3]. Yet meeting this target alone is not enough: SMMs in electrical engines must withstand severe mechanical loads; that is, the alloys need high strength and ductility[4]. This is a fundamental design challenge, as most methods that enhance strength introduce stress fields that can pin magnetic domains, thus increasing coercivity and hysteresis losses[5]. Here we introduce an approach to overcome this dilemma. We have designed a Fe–Co–Ni–Ta–Al multicomponent alloy (MCA) with ferromagnetic matrix and paramagnetic coherent nanoparticles (about 91 nm in size and around 55% volume fraction). They impede dislocation motion, enhancing strength and ductility. Their small size, low coherency stress and small magnetostatic energy create an interaction volume below the magnetic domain wall width, leading to minimal domain wall pinning, thus maintaining the soft magnetic properties. The alloy has a tensile strength of 1,336 MPa at 54% tensile elongation, extremely low coercivity of 78 A m^{-1} (less than 1 Oe), moderate saturation magnetization of 100 A m^2 kg^{-1} and high electrical resistivity of 103 μΩ cm.

Lowest possible coercivity and highest possible electrical resistivity are primary goals for SMMs, to reduce hysteresis-related and eddy-current-related energy losses, noise and the associated material damage[1–3]. Also, new SMMs with higher strength and ductility are needed, to operate under mechanically demanding loading conditions for safety-critical parts in transport and energy[4]. High strength and ductility also serve as measures for many other mechanical properties, such as high hardness[5] and fracture toughness[6]. This multi-property profile creates a fundamental dilemma. The mechanical strength of metallic materials is produced by lattice defects and their elastic interactions with linear lattice faults that carry inelastic deformation, referred to as dislocations. However, the defects also interact with the magnetic domain walls and pin them. The loss in domain wall motion increases coercivity, so that the materials lose their soft magnetic features. Therefore, current SMMs follow the design rule of avoiding lattice defects to minimize coercivity[7]. On the other hand, increasing the mechanical strength of an alloy requires enhancing its internal stress level through defects such as dislocations, grain boundaries and precipitates[8]. This means that the task of making soft magnets mechanically strong is a trade-off between two mutually exclusive design strategies, namely, mechanical strength versus unaffected domain wall motion.

The theory of the grain size dependence of coercivity[9] shows its proportionality to the sixth power of the grain size for the case of nanocrystalline materials, a relation that can also be applied to particles[10]. Current design of SMMs has thus focused on using small particles (less than 15 nm)[10,11] and grain sizes (less than 100 nm)[12–14]. According to magnetic strain theory, the coercivity depends on the energy required to displace domain walls to overcome lattice barriers[15]. Here we introduce particles into a multicomponent massive solid solution matrix and increase their size from the commonly used range of 5–15 nm to 90–100 nm. With that, the internal stress level and the overall elastic coherency misfit energy are reduced through the smaller specific surface area (total surface area per unit of volume) of the particles, caused by the coarsening. We then propose that the particle design must follow four main rules. First, minimal pinning of domain walls requires a well-tuned and well-controlled particle size distribution with optimum balance between the decrease in specific surface area and the increase in magnetostatic energy during particle coarsening. Second, the particle size must remain smaller than the domain wall width to prevent strong pinning, that is, strong resistance against spin rotation[8]. Third, the chemical composition and crystal structure of the particles determine their saturation magnetization; therefore, antiferromagnetic elements are usually excluded. Fourth, strengthening of the alloys is determined by the interaction between dislocations and particles and by the friction forces exerted on dislocations in the massive solid solution matrix. Thus, intrinsically strong intermetallic particles with minimal lattice misfit are targeted. These require high forces for dislocation cutting (providing strength), but repeated cutting

[1]Max-Planck-Institut für Eisenforschung, Düsseldorf, Germany. [2]Department of Materials Science, Technical University of Darmstadt, Darmstadt, Germany. [3]School of Materials Science and Engineering, Central South University, Changsha, China. ✉e-mail: lizhiming@csu.edu.cn; d.raabe@mpie.de

a Inverse pole figure — 100 μm

b ECC image — 5 μm

c Measured / fcc (Pm-3m, simulated) / L1$_2$ (Fm-3m, simulated) / Cubic (Fd-3m, simulated)

d Dark-field TEM — 100 nm

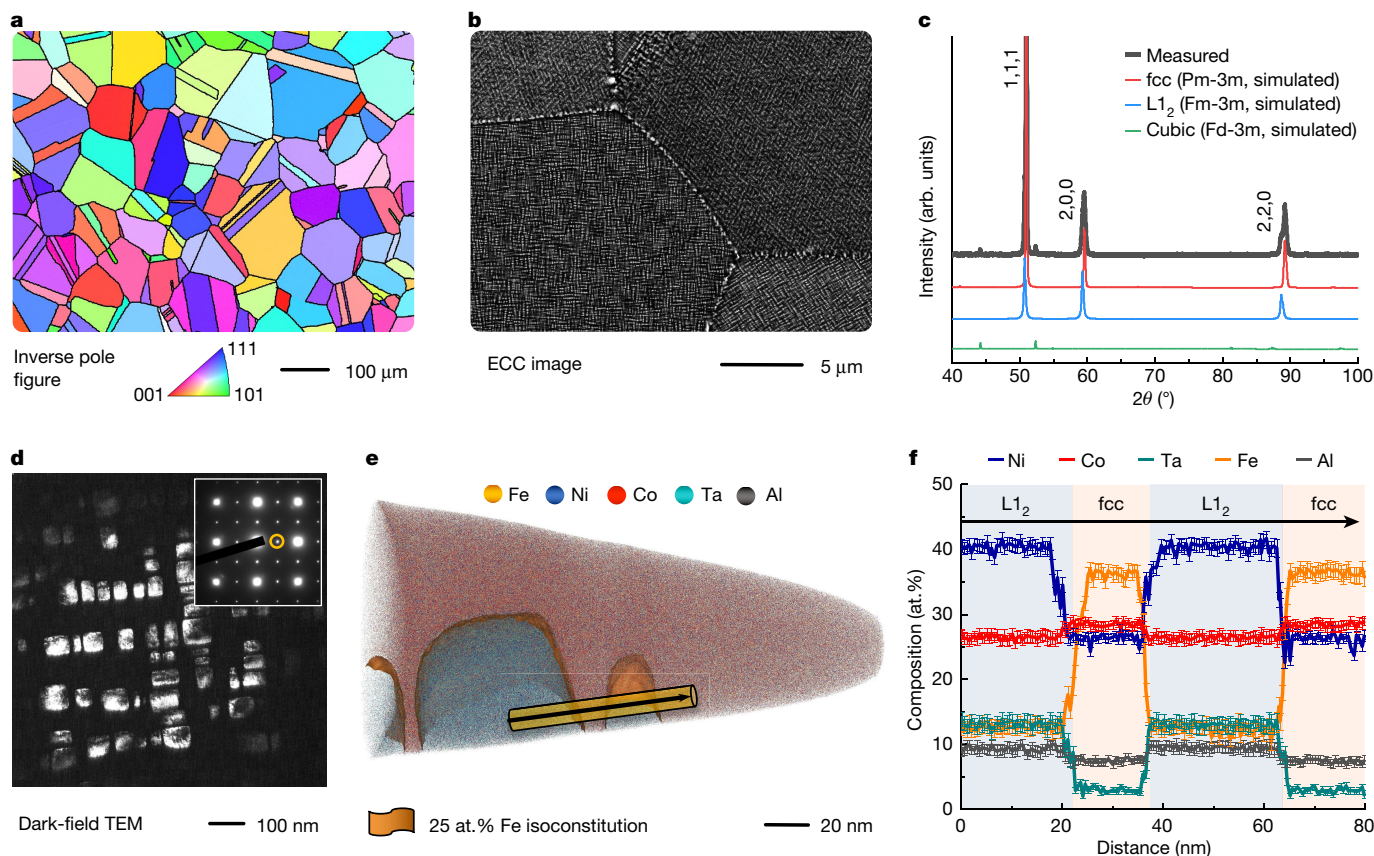e Fe Ni Co Ta Al · 25 at.% Fe isoconstitution — 20 nm

f Ni Co Ta Fe Al

Fig. 1 | Microstructure and chemical composition of the M-MCA. a, EBSD inverse pole figure map showing the equiaxed grains of the fcc matrix. The black lines highlight the high-angle grain/twin boundaries. **b**, ECC image featuring the high-density uniformly distributed L1$_2$ particles in the grain interiors and heterogeneous particles at the grain boundaries. **c**, Measured and simulated XRD patterns showing the phase structures. **d**, Centred DF-TEM image of the L1$_2$ particles obtained using the (011) superlattice spot (see inset).

e, 3D reconstruction map of a typical APT tip showing the cuboidal L1$_2$ particles embedded in the fcc matrix. The L1$_2$–fcc interfaces are highlighted using isocomposition surfaces containing 25 at.% Fe. **f**, 1D compositional profiles computed along the cylinder region in **e** (marked by the black arrow), showing the compositional changes across several interfaces. Error bars refer to the standard deviations of the counting statistics in each bin of the profiles.

by ensuing dislocations emitted by the same source shear them with gradual ease along the remaining and gradually reducing particle cross sections (providing ductility).

These different mechanism considerations had to be translated into a corresponding compositional alloy design concept. This is mainly guided by the requirement for (1) a ferromagnetic matrix with (2) high solid solution contribution and components that trigger the formation of (3) strong and stable intermetallic phases with (4) small lattice misfit relative to the matrix. These considerations have led us to the non-equiatomic iron–nickel–cobalt–tantalum–aluminium (Fe$_{32.6}$Ni$_{27.7}$Co$_{27.7}$Ta$_{5.0}$Al$_{7.0}$ (at.%)) MCA. We synthesized the material in a vacuum induction melting furnace, followed by conventional hot rolling and homogenization (details of the processing procedures and chemical compositions are provided in Methods). Through further isothermal heat treatments (1–100 h at 1,173 K), we prepared samples with different average particle sizes, ranging from 24 ± 15 nm to 255 ± 49 nm (edge length is used to characterize the topological particle size). The particles have L1$_2$ structure and complex composition, as presented in detail below.

Microstructure analysis

Figure 1 shows the structural characterization of the MCA with medium particle size (M-MCA, in which 'M' stands for medium particle size) after annealing at 1,173 K for 5 h. The M-MCA shows an average grain size of 85.3 ± 25.6 μm (excluding annealing twin boundaries) according

to electron backscatter diffraction (EBSD) analysis shown in Fig. 1a. The electron channelling contrast imaging (ECCI) analysis shows that the L1$_2$ particles have a high number density (7.2 ± 0.2) × 10^{20} m^{-3} and a large volume fraction (55 ± 1%) in homogeneous distribution within the face-centred cubic (fcc) matrix (Fig. 1b). The lattice misfit (0.48%) between the fcc matrix and the L1$_2$ particles has been calculated using their lattice parameters acquired from the X-ray diffraction (XRD) patterns (Fig. 1c) by Rietveld simulation. Such a small lattice mismatch reduces the driving forces for further coarsening and the uniform dispersion prevents plastic localization at high strength[16]. The central beam dark-field (DF) transmission electron microscopy (TEM) analysis shows that the average size of the L1$_2$ particles is 90.8 ± 35.8 nm (Fig. 1d). The corresponding selected-area electron diffraction (see inset of Fig. 1d) and high-resolution (HR)-TEM (Extended Data Fig. 1d) confirm the high coherency between the particles and the matrix.

The elemental partitioning between the L1$_2$ precipitates and fcc solid solution matrix is characterized by atom probe tomography (APT). Figure 1e shows the 3D distribution of the volume investigated by APT, highlighted by a set of isosurfaces delineating regions containing more than 25 at.% Fe. Figure 1f shows the 1D compositional profiles acquired along the cylinder in Fig. 1e. The profiles show that Fe partitions into the fcc matrix (36 at.%), whereas the L1$_2$ particles are enriched in Ni (40 at.%), Ta (13 at.%) and Al (9 at.%). The compositions of the fcc and L1$_2$ phases were determined by averaging over three APT datasets (including ten L1$_2$ particles) as Fe$_{36}$Co$_{28}$Ni$_{26}$Al$_7$Ta$_3$ and Ni$_{40}$Co$_{26}$Ta$_{13}$Fe$_{12}$Al$_9$ (at.%), respectively.
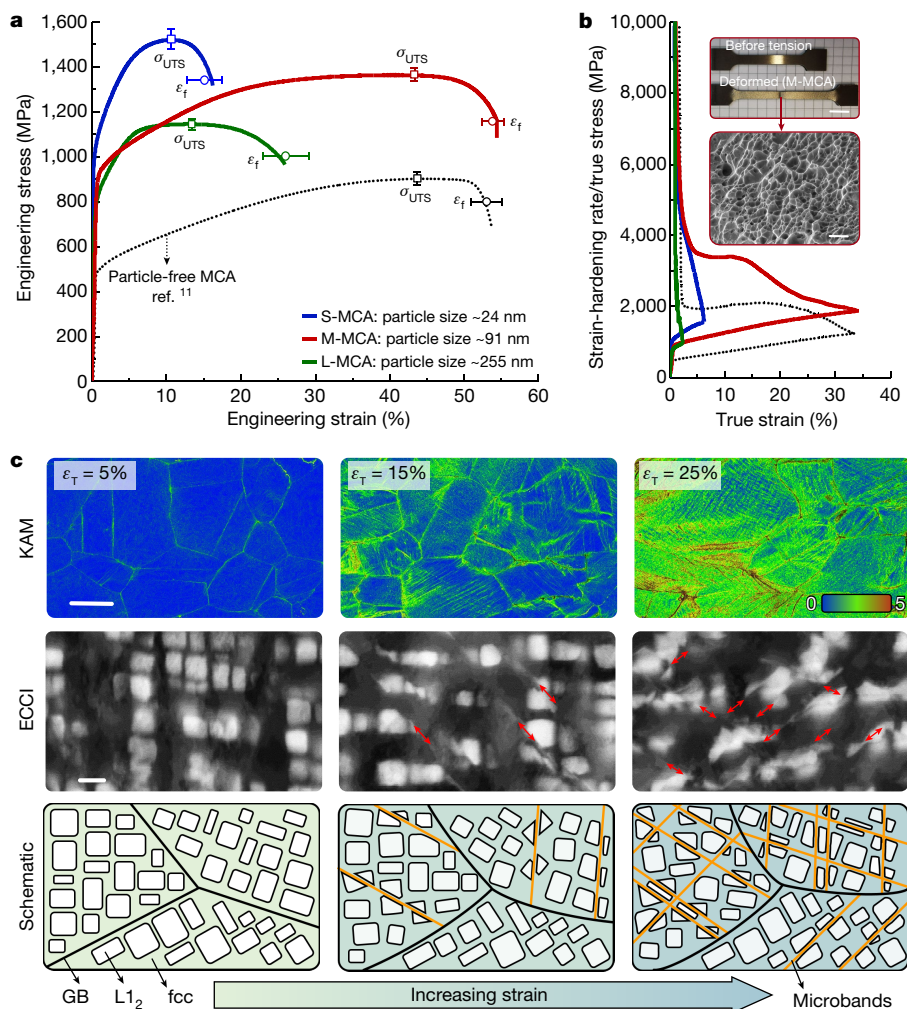
Fig. 2 | Mechanical behaviour and nanoscale processes during plastic straining of the M-MCA. a, Typical engineering stress–strain curves measured at room temperature, together with the average values for ultimate tensile strength (σ_{UTS}) and elongation at fracture (ε_f). **b**, Strain-hardening rate/true stress–true strain curves. The insets show the macroscopic image (top inset; scale bar, 1 cm) of the tensile sample and the corresponding fracture morphology (bottom inset; scale bar, 5 µm), in which a typical ductile fracture with fine dimples is observed. **c**, Substructure evolution as a function of global strain observed after interrupted tensile tests: EBSD-KAM maps showing the distributions of deformation-induced misorientations (top images; scale bar, 50 µm), in which ε_T stands for the global true strain; ECCI analysis (middle images; scale bar, 100 nm) showing the evolution of microbands; the shearing of L1$_2$ particles is highlighted by red arrows; schematics (bottom images) illustrating the microband refinement in the M-MCA during plastic straining.

Apart from these intragranular nanoparticles, we also observed two types of grain boundary variants: (1) coarse grain boundary particles (160.2 ± 55.3 nm) with the same crystal structure and composition as those inside the grains (Extended Data Fig. 1a–c) and (2) incoherent particles with a minor fraction (less than 0.3%) at the triple points of the grains with different structure (cubic Fd-3m, Fig. 1c) and composition ($Ta_{40}Co_{26}Fe_{20}Ni_{11}Al_3$ (at.%), Extended Data Fig. 1e). These two types of particle are promoted by the high diffusion rate along the grain boundaries.

Mechanical properties

The current strategy of tuning the particle size also allows overcoming the strength–ductility trade-off, which is notable for advanced alloys with gigapascal-level strength. Figure 2a shows the tensile stress–strain curves of the M-MCA at room temperature (red curve). The yield strength (σ_y) is 904 ± 11 MPa, with an ultimate tensile strength (σ_{UTS}) of 1,336 ± 21 MPa and an elongation at fracture (ε_f) up to 53.6 ± 1.5%, averaged from four tests. Accordingly, the M-MCA has a high $\sigma_{UTS} \times \varepsilon_f$ value of 71.6 GPa%. To show the improvement in strength and ductility achieved by the well-controlled particle size distribution, the

mechanical response of a material variant with identical chemical composition, that is, $Fe_{32}Co_{28}Ni_{28}Ta_5Al_7$ (at.%), but smaller particle size (S-MCA, annealed for 1 h, producing an average particle size of 24 nm), larger particle size (L-MCA, annealed for 100 h, average particle size of 255 nm) and the particle-free $Fe_{35}Co_{30}Ni_{30}Ta_5$ (at.%) alloy[11] are also presented in Fig. 2a.

Compared with the single-phase $Fe_{35}Co_{30}Ni_{30}Ta_5$ (at.%) alloy with a relatively low value of σ_y of 501 MPa (ref. [11]), the notable increase in yield strength of the M-MCA can be attributed to the precipitation strengthening of the L1$_2$ particles with a high volume fraction (55%). Especially, such an improvement in the strength of the M-MCA is achieved at no expense of ductility, which is fundamentally different from the case of the S-MCA, in which a pronounced loss in ductility is observed with increasing strength. The good ductility is correlated with the high work-hardening capability, as shown in Fig. 2b. Further increase of particle size at longer annealing time (100 h) in the L-MCA leads to the decrease of ductility (53%) and σ_{UTS} (14%) as compared with those of the M-MCA. This is related to the mechanical weakness, strain localization and embrittlement in the particle-free zone adjacent to the grain boundary caused by solute depletion (Extended Data Fig. 2a). This interfacial weakening has been confirmed by the associated fracture
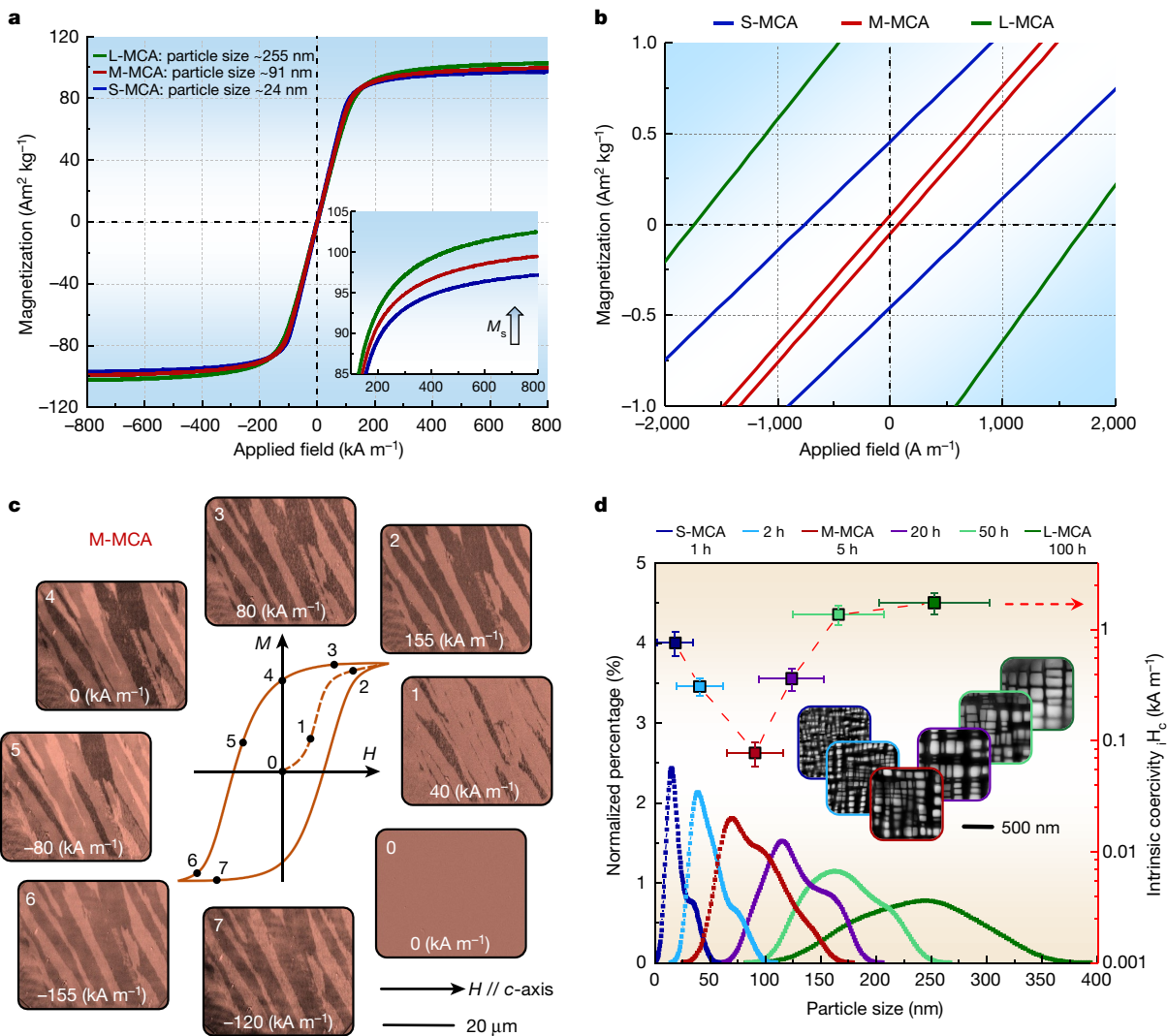
Fig. 3 | Soft magnetic response and associated Bloch wall motion behaviour of the MCAs at room temperature. a, Hysteresis loops (*M/H*) acquired up to ±800 kA m⁻¹. The magnetic-field-sweeping rate is 1 kA m⁻¹. The inset shows the enlarged view of the increase in saturation magnetization with particle coarsening. **b**, *M/H* curves measured at a rate of 0.1 kA m⁻¹ between ±50 kA m⁻¹, showing the extremely low coercivity. **c**, MOKE microscopy observation, in longitudinal contrast, showing the magnetization process. The applied magnetic field is horizontal to the viewing plane. **d**, Statistical particle size distribution of all the MCAs under different isothermal heat treatment conditions (1–100 h at 1,173 K). The inset shows the evolution of particle size by ECCI probing.

morphologies, with typical ductile fracture with fine dimples in the M-MCA material (see Fig. 2b inset) and intergranular fracture in the L-MCA material (Extended Data Fig. 2b).

To unravel the mechanisms responsible for the marked improvement in the strength–ductility combination of the M-MCA, we studied its deformation substructures using EBSD kernel average misorientation (KAM) analysis and ECCI at different hardening stages (Fig. 2c). In principle, high strength requires to impede dislocation movement, whereas good ductility needs mobility of dislocations and new production of dislocations[17]. At the early deformation stage, the M-MCA deforms by planar dislocation glide on {111} planes (Extended Data Fig. 3a–c), as commonly observed in fcc alloys[18]. The dislocations extend through the grains. Corresponding pile-up configurations at the grain boundaries are shown by the higher KAM values (for example, at $\varepsilon_T = 5\%$; see KAM maps in Fig. 2c). The relatively large grain size (85.3 µm) of the current M-MCA enables higher mobility of dislocations compared with most of the previously reported strong MCAs that had smaller grain size[19–21] (around 10 µm). Further straining refines the crystallographically aligned microbands and facilitates the shearing of L1₂ particles (for example, at $\varepsilon_T = 15\%$; see ECC images in Fig. 2c).

The quantification of the evolution of the average microband spacing shows a microband refinement process during straining (Extended Data Fig. 3d). The gradually reduced microband spacing causes higher passing stress and, thus, enhanced strain hardening. This has been proposed to explain the good strength–ductility combinations in high-manganese steels[22] and MCAs[23]. Hence, the observed dynamic microband refinement and particle shearing are the prevalent deformation mechanisms in the current MCAs. No Orowan looping was observed, even when increasing the average particle size up to 255 nm for the L-MCA (Extended Data Fig. 2c), as the average particle spacing remains far below the critical value (3,094 nm, see Methods) for the activation of dislocation bowing around particles, a mechanism referred to as Orowan effect. Furthermore, the stress required for shearing particles in the M-MCA with a medium particle size (91 nm) with high volume fraction (55%) is 2.2 times larger than that for the S-MCA with a smaller particle size (24 nm) with low volume fraction (43 ± 1%) (see Extended Data Table 1). Therefore, the high critical shear stress required for cutting the L1₂ particles and the dynamic microband refinement during plastic deformation lead to the strong strain-hardening capacity of the M-MCA.
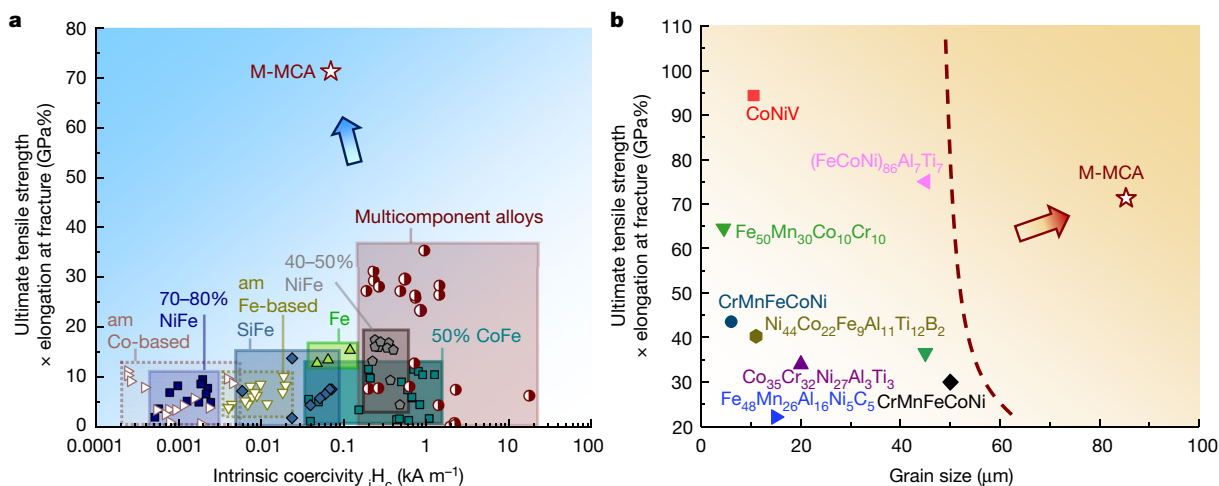
Fig. 4 | Mechanical and magnetic features combined in the new Fe$_{32}$Co$_{28}$Ni$_{28}$Ta$_5$Al$_7$ (at.%) M-MCA material. a, Ashby map compiling room-temperature ultimate tensile strength (σ_{UTS}) × elongation at fracture (ε_f) and intrinsic coercivity compared with other SMMs, such as Fe–Ni (refs. [24,25]), Fe–Si (refs. [38]), Fe–Co (refs. [39,40]), Fe (ref. [41]), amorphous alloys[42–45] and established MCAs[26–37]. **b**, Ashby map showing σ_{UTS} × ε_f values versus average grain size compared with data for other strong and ductile MCAs[16,19–21,47–50]. am, amorphous alloys.

Magnetic properties

Figure 3a,b shows the magnetic properties of the MCAs. All alloys show typical soft ferromagnetic behaviour. The M-MCA shows an excellent combination of extremely low coercivity (H_c) of 78 ± 3 A m^{-1} (less than 1 Oe) and moderate saturation magnetization (M_s) of 100.2 ± 0.2 A m^2 kg^{-1}. We identified a higher M_s for the alloy variant with larger average particle size (see inset in Fig. 3a). The reason for this is the change in intrinsic magnetic behaviour, as indicated by the higher Curie temperature (T_c), shown by the thermomagnetic curves (Extended Data Fig. 4a). Two distinct changes of the slope, indicating two ferromagnetic phases, are observed in the S-MCA. By contrast, only one sharp drop is observed in the M-MCA and L-MCA materials, indicating the presence of only one ferromagnetic phase. This is further confirmed by measuring the magnetic behaviour of the MCAs at elevated temperatures (Extended Data Fig. 4b). Considering that both the fcc and L1$_2$ phases contain high concentrations of ferromagnetic elements, we investigated their individual magnetic response through casting both phases as separate bulk samples with their respective nominal compositions acquired previously from APT analysis (see Methods for details). The results show that the L1$_2$ bulk phase is paramagnetic, whereas the fcc matrix is ferromagnetic in the M-MCA (Extended Data Fig. 4c). Owing to different partitioning, the magnetic behaviour of the L1$_2$ phase varies from ferromagnetic in the S-MCA material variant to paramagnetic in the M-MCA and L-MCA materials. The mechanism behind this transition is the change in the intrinsic spin alignment, which is related to the change in chemical composition (Extended Data Fig. 5) and ordering during annealing. The overall increase in saturation magnetization of the MCAs as a function of particle coarsening is attributed to the change in fcc matrix composition owing to elemental partitioning (Extended Data Fig. 5), that is, specifically to the resultant higher concentration of (Fe+Co) in the fcc matrix. This effect enhances the total average magnetic moment per formula unit and leads to a higher M_s.

To gain further insight into the mechanism behind the magnetic response of the M-MCA, we investigated the domain structure using magneto-optical Kerr effect (MOKE) microscopy (Fig. 3c) under different applied magnetic field strengths. Starting from the AC demagnetized state to an applied field of 40 kA m^{-1}, the nucleation of magnetic domains is uniformly distributed within the grain. Further increasing the applied field (155 kA m^{-1}) leads to domain wall movement and growth of

energetically favourable domains. The domains grow unaffected inside the grains but get impeded at grain and twin boundaries (Extended Data Fig. 6). Figure 3d summarizes the statistically averaged particle size distribution with respect to the coercivity of all the MCA samples at different annealed states. The data are acquired by developing an automated processing protocol, as shown in Extended Data Fig. 7. The coercivity first decreases from 763 A m^{-1} (S-MCA, average particle size 24 nm) to 78 A m^{-1} (M-MCA, average particle size 91 nm) and then increases to 1,745 A m^{-1} (L-MCA, average particle size 255 nm). Both the average particle size and the grain size increase monotonously with increasing annealing time (Extended Data Table 1). Because the grain size of the MCAs material is above the critical single-domain size, its coercivity decreases with grain coarsening, following the model for the grain size dependence of the coercivity as $H_c \propto 1/D$ (in which D is the grain size)[13]. However, the magnitude of the decrease in coercivity owing to grain coarsening according to the model is negligible compared with the experimentally observed values: the difference according to the model calculation between the S-MCA and M-MCA material variants is 2 A m^{-1}, but the experimentally observed difference is 775 A m^{-1}. Accordingly, the energy required for the irreversible displacement of domain walls within the grain is the determining effect for the extremely low coercivity.

Therefore, the notable decrease in coercivity at the early particle coarsening stage (≤91 nm) is attributed to the gradual reduction of the overall coherency stresses between matrix and particles, owing to their average size increase. More specifically, the values of the specific surface area × integrated lattice misfit decrease from 1.09 × 10^6 m^{-1} in the S-MCA material to 4.08 × 10^5 m^{-1} in the M-MCA material. The dislocation density in the matrix decreases from 1.50 × 10^{14} m^{-2} in the S-MCA material to 9.32 × 10^{13} m^{-2} in the M-MCA material when increasing the annealing time from 1 h to 5 h (see Methods). The reduction in dislocation density lowers the associated elastic distortion fields that can pin the domain walls. Although the elastic distortion and dislocation density decrease with particle coarsening, the coercivity of the L-MCA material increases. Two main mechanisms are proposed to explain this. First, the average particle size and the associated strain field in the L-MCA becomes larger than the domain wall width (δ_w), leading to domain wall pinning. The L-MCA has a δ_w of 117 nm and a much larger average particle size of 255 nm, whereas the average particle size of the M-MCA is 91 nm, which is below its δ_w of 112 nm (see Methods). Second, the increased magnetostatic energy (E_s) associated with the paramagnetic particles causes a stronger individual pinning effect of each particle

on the domain wall motion. More specifically, the E_s of the L-MCA is estimated to be 23 times larger than that of the M-MCA (see Methods). When considering only particle size, it should be noted that, for the M-MCA, the coherent particles distributed along the grain boundaries with an average size (160 nm) above the δ_w (112 nm) are expected to have a stronger pinning effect on the domain walls than those in the grain interiors (91 nm). However, these coarser particles occupy only a small fraction (1.2 ± 0.2% in M-MCA), hence, with a negligible effect on domain wall motion.

These considerations show that the nanoscale size distribution of the particles must be carefully controlled to minimize their pinning effect on domain wall movement, which determines the coercivity of the alloy. This is achieved here by an optimal balance between the release of structural defects (for example, interfacial elastic distortion, dislocation density) just down to a level required to maintain high mechanical strength and the increase of the pinning effect from the magnetostatic energy, while keeping the particle size below the domain wall width during particle coarsening.

Overview of several property profiles

To highlight the good combination of mechanical and magnetic properties of the M-MCA with optimal particle size, we compare it with existing SMMs in an Ashby plot showing the $\sigma_{UTS} \times \varepsilon_f$ values against the H_c (Fig. 4a). This comparison shows that the $\sigma_{UTS} \times \varepsilon_f$ value of the new M-MCA material outperforms all other SMMs. Notably, the H_c of the new material is lower than that of all Fe–Ni (refs. [24,25]) alloys and other MCAs[26–37], comparable with that of Fe–Si (ref. [38]), Fe–Co (refs. [39,40]) alloys and pure Fe (ref. [41]). Amorphous and nanocrystalline soft magnetic alloys[42–45] can show ultralow H_c (less than 10 A m^{-1}) and high mechanical strength, yet their limited ductility, damage tolerance and workability prohibit their application in cases in which the load path changes or high stresses, forming or machining are applied. A radar plot comparing the various soft magnetic and mechanical properties of the current M-MCA with several typical commercial SMMs is shown in Extended Data Fig. 8. Although the saturation induction (B_s) of the current M-MCA is not comparable with that of typical commercial SMMs (Extended Data Fig. 9), it has higher electrical resistivity (ρ) (103 ± 0.8 μΩ cm, see Extended Data Fig. 10), a feature that makes it suited for applications with AC conditions. The high ρ of the M-MCA is expected to be derived from the high resistance to electron movement from the larger lattice distortion[46]. Figure 4b compares the $\sigma_{UTS} \times \varepsilon_f$ values versus the grain size of the M-MCA material with recently reported strong and ductile MCAs[16,19–21,47–50]. The analysis shows that the current alloy reaches high values of $\sigma_{UTS} \times \varepsilon_f$ even without the substantial contribution from grain boundaries, confirming the notable strengthening effect provided by the nanoparticles and the massive solid solution.

Conclusions

In summary, we have developed a material that unifies so far mutually exclusive properties, namely, high mechanical strength (1,336 MPa), high tensile ductility (54%), low coercivity (78 A m^{-1}), moderate saturation magnetization (100 A m^2 kg^{-1}) and high resistivity (103 μΩ cm). We realized this in a new class of bulk SMMs through a nanoparticle dispersion with well-controlled size (91 nm), magnetic properties, coherency strain, strength and interface energy. The design strategy is opposite to that generally applied in conventional SMM design. Instead of using the smallest microstructure features (particle size <15 nm) to avoid magnetic wall pinning as in conventional SMMs, we have chosen a relatively coarse particle dispersion with tuned particle/matrix interfacial coherency stresses and paramagnetic properties to minimize magnetic pinning of domain walls on the one hand (soft magnetism) and maximize interaction strength with dislocations on the other (strength and ductility).

The infinite composition space of MCAs allows realizing materials with good combinations of soft magnetic and mechanical properties. The new alloy design approach allows for tailoring SMMs for magnetic parts exposed to severe mechanical loads, be it from manufacturing and/or during service, for which conventional SMMs are mechanically too soft or too brittle. Future efforts on developing advanced magnetic MCAs could target variants with further improved soft magnetic properties (for example, higher magnetic saturation) while preserving their outstanding mechanical properties, at lower alloy costs, and use high-throughput experiments combined with computational techniques, for example, machine learning, to accelerate the discovery of new alloy variants.

Online content

Any methods, additional references, Nature Research reporting summaries, source data, extended data, supplementary information, acknowledgements, peer review information; details of author contributions and competing interests; and statements of data and code availability are available at https://doi.org/10.1038/s41586-022-04935-3.

1. Silveyra, J. M. et al. Soft magnetic materials for a sustainable and electrified world. *Science* **362**, eaao0195 (2018).
2. Krings, A. et al. Soft magnetic material status and trends in electric machines. *IEEE Trans. Ind. Electron.* **64**, 2405–2414 (2017).
3. Gutfleisch, O. et al. Magnetic materials and devices for the 21st century: stronger, lighter, and more energy efficient. *Adv. Mater.* **23**, 821–842 (2011).
4. Henke, M. et al. Challenges and opportunities of very light high-performance electric drives for aviation. *Energies* **11**, 344 (2018).
5. Zhang, P. et al. General relationship between strength and hardness. *Mater. Sci. Eng. A* **529**, 62–73 (2011).
6. Hofmann, D. et al. Designing metallic glass matrix composites with high toughness and tensile ductility. *Nature* **451**, 1085–1089 (2008).
7. Hasegawa, T. et al. Conversion of FeCo from soft to hard magnetic material by lattice engineering and nanopatterning. *Sci. Rep.* **7**, 13125 (2017).
8. Cullity, B. D. & Graham, C. D. *Introduction to Magnetic Materials* 2nd edn (Wiley-IEEE Press, 2008).
9. Herzer, G. Grain size dependence of coercivity and permeability in nanocrystalline ferromagnets. *IEEE Trans. Magn.* **26**, 1397–1402 (1990).
10. Ma, Y. et al. A novel soft-magnetic B2-based multiprincipal-element alloy with a uniform distribution of coherent body-centered-cubic nanoprecipitates. *Adv. Mater.* **33**, 2006723 (2021).
11. Han, L. et al. Ultrastrong and ductile soft magnetic high-entropy alloys via coherent ordered nanoprecipitates. *Adv. Mater.* **33**, 2102139 (2021).
12. Fu, Z. et al. Exceptional combination of soft magnetic and mechanical properties in a heterostructured high-entropy composite. *Appl. Mater. Today* **15**, 590–598 (2019).
13. Herzer, G. Grain structure and magnetism of nanocrystalline ferromagnets. *IEEE Trans. Magn.* **25**, 3327–3329 (1989).
14. Osaka, T. et al. A soft magnetic CoNiFe film with high saturation magnetic flux density and low coercivity. *Nature* **392**, 796–798 (1998).
15. Miyazaki, T. & Jin, H. *The Physics of Ferromagnetism* (Springer, 2012).
16. Yang, T. et al. Multicomponent intermetallic nanoparticles and superb mechanical behaviors of complex alloys. *Science* **362**, 933–937 (2018).
17. Tolansky, S. Dislocations. *Nature* **209**, 1058–1059 (1966).
18. Pande, C. S. & Hazzledine, P. M. Dislocation arrays in Cu-Al alloys. II. *Philos. Mag.* **24**, 1393–1410 (1971).
19. Yang, T. et al. Ultrahigh-strength and ductile superlattice alloys with nanoscale disordered interfaces. *Science* **369**, 427–432 (2020).
20. Luo, H. et al. A strong and ductile medium-entropy alloy resists hydrogen embrittlement and corrosion. *Nat. Commun.* **11**, 3081 (2020).
21. Wang, Z. et al. Ultrastrong lightweight compositionally complex steels via dual-nanoprecipitation. *Sci. Adv.* **6**, eaba9543 (2020).
22. Welsch, E. et al. Strain hardening by dynamic slip band refinement in a high-Mn lightweight steel. *Acta Mater.* **116**, 188–199 (2016).
23. Wang, Z. et al. The effect of carbon on the microstructures, mechanical properties, and deformation mechanisms of thermo-mechanically treated Fe$_{40.4}$Ni$_{11.3}$Mn$_{34.8}$Al$_{7.5}$Cr$_6$ high entropy alloys. *Acta Mater.* **126**, 346–360 (2017).
24. Christenson, T. R. et al. Mechanical and metallographic characterization of LIGA fabricated nickel and 80%Ni-20%Fe permalloy. *MRS Online Proc. Libr.* **518**, 185–190 (1998).
25. Yekta, P. V. et al. Magnetic and mechanical properties of cold-rolled permalloy. *J. Magn. Magn. Mater.* **468**, 155–163 (2018).
26. Zhang, Y. et al. High-entropy alloys with high saturation magnetization, electrical resistivity and malleability. *Sci. Rep.* **3**, 1455 (2013).
27. Körmann, F. et al. "Treasure maps" for magnetic high-entropy-alloys from theory and experiment. *Appl. Phys. Lett.* **107**, 142404 (2015).
28. Li, P. et al. A ductile high entropy alloy with attractive magnetic properties. *J. Alloys Compd.* **694**, 55–60 (2017).
29. Zuo, T. T. et al. Effects of Al and Si addition on the structure and properties of CoFeNi equal atomic ratio alloy. *J. Magn. Magn. Mater.* **371**, 60–68 (2014).

Article

30. Wang, Y. P. et al. Solid solution or intermetallics in a high-entropy alloy. *Adv. Eng. Mater.* **11**, 641–644 (2009).

31. Zhang, K. B. et al. Annealing on the structure and properties evolution of the CoCrFeNiCuAl high-entropy alloy. *J. Alloys Compd.* **502**, 295–299 (2010).

32. Ma, S. G. & Zhang, Y. Effect of Nb addition on the microstructure and properties of AlCoCrFeNi high-entropy alloy. *Mater. Sci. Eng. A* **532**, 480–486 (2012).

33. Zhang, K. & Fu, Z. Effects of annealing treatment on properties of CoCrFeNiTiAl$_x$ multi-component alloys. *Intermetallics* **28**, 34–39 (2012).

34. Na, S. M. et al. Room-temperature ferromagnetic transitions and the temperature dependence of magnetic behaviors in FeCoNiCr-based high-entropy alloys. *AIP Adv.* **8**, 056412 (2018).

35. Duan, H. et al. Al addition effect on structure and magnetic properties in high B_s Fe-Cu-Si-B alloys. *Mater. Res. Bull.* **111**, 289–293 (2019).

36. Zhang, H. et al. A novel FeCoNiCr$_{0.2}$Si$_{0.2}$ high entropy alloy with an excellent balance of mechanical and soft magnetic properties. *J. Magn. Magn. Mater.* **478**, 116–121 (2019).

37. Zuo, T. et al. Novel high entropy alloys of Fe$_x$Co$_{1-x}$NiMnGa with excellent soft magnetic properties. *Intermetallics* **100**, 1–8 (2018).

38. Chen, C. W. *Magnetism and Metallurgy of Soft Magnetic Materials* (Dover, 2013).

39. George, E. P. et al. Mechanical properties of soft magnetic FeCo alloys. *Mater. Sci. Eng. A* **329**, 325–333 (2002).

40. Bozorth, R. M. *Ferromagnetism* (Wiley, 1993).

41. Pepperhoff, W. & Acet, M. *Constitution and Magnetism of Iron and its Alloys* (Springer, 2001).

42. Inoue, A. et al. Cobalt-based bulk glassy alloy with ultrahigh strength and soft magnetic properties. *Nat. Mater.* **2**, 661–663 (2003).

43. Inoue, A. et al. Ultra-high strength above 5000 MPa and soft magnetic properties of Co–Fe–Ta–B bulk glassy alloys. *Acta Mater.* **52**, 1631–1637 (2004).

44. Lin, C. Y. et al. Fe–Y–M–B (M = Nb or Ta) bulk metallic glasses with ultrahigh strength and good soft magnetic properties. *J. Phys. D Appl. Phys.* **40**, 310–314 (2007).

45. Shen, B. et al. Superhigh strength and good soft-magnetic properties of (Fe,Co)–B–Si–Nb bulk glassy alloys with high glass-forming ability. *Appl. Phys. Lett.* **85**, 4911–4913 (2004).

46. Yan, X. & Zhang, Y. Functional properties and promising applications of high entropy alloys. *Scr. Mater.* **187**, 188–193 (2020).

47. Li, Z. et al. Metastable high-entropy dual-phase alloys overcome the strength–ductility trade-off. *Nature* **534**, 227–230 (2016).

48. Du, X. H. et al. Dual heterogeneous structures lead to ultrahigh strength and uniform ductility in a Co-Cr-Ni medium-entropy alloy. *Nat. Commun.* **11**, 2390 (2020).

49. Gludovatz, B. et al. A fracture-resistant high-entropy alloy for cryogenic applications. *Science* **345**, 1153–1158 (2014).

50. Otto, F. et al. The influences of temperature and microstructure on the tensile properties of a CoCrFeMnNi high-entropy alloy. *Acta Mater.* **61**, 5743–5755 (2013).

Methods

Materials preparation

The bulk MCA ingot with a predetermined nominal composition of $Fe_{32.6}Co_{27.7}Ni_{27.7}Ta_{5.0}Al_{7.0}$ (at.%) was first cast in a vacuum induction furnace using pure metallic ingredients (purity higher than 99.8 wt.%) under high-purity argon (Ar) atmosphere. The as-cast ingot with dimension 40 mm × 60 mm × 20 mm (length × width × thickness) was then hot rolled at 1,473 K to an engineering thickness reduction of 50% (final thickness 10 mm). After hot rolling, the alloy sheets were then homogenized at 1,473 K for 10 min in Ar atmosphere, followed by water quenching. To obtain a wide size distribution of the particles, further isothermal heat treatments were conducted at 1,173 K, lasting from 1 h up to 100 h (1 h, 2 h, 5 h, 20 h, 50 h and 100 h) in Ar atmosphere and followed by water quenching. The exact chemical composition of the MCA measured by wet-chemical analysis is $Fe_{32.0}Co_{28.0}Ni_{28.1}Ta_{4.7}Al_{7.2}$ (at.%), which is close to the predesigned composition. In addition, the bulk ingots (50 g) with compositions identical to that of the fcc ($Fe_{36}Co_{28}Ni_{26}Al_7Ta_3$ (at.%)) matrix phase and the $L1_2$ particle ($Ni_{40}Co_{26}Ta_{13}Fe_{12}Al_9$ (at.%)) in the M-MCA derived from the APT analysis were also cast, respectively, by arc melting under Ar atmosphere. The ingots were remelted six times to achieve chemical homogeneity.

Analytical methods

XRD measurements were carried out in an X-ray system (Diffractometer D8 Advance A25-X1) with Co Kα radiation ($\lambda = 1.78897$ Å, 35 kV and 40 mA). EBSD characterizations were conducted in a ZEISS Crossbeam focused ion beam scanning electron microscope at 15 kV. ECCI characterizations were performed using a ZEISS MERLIN high-resolution field-emission electron microscope at 30 kV. TEM analysis including selected-area electron diffraction was conducted in a JEOL JEM-2100 at 200 kV. Scanning transmission electron microscopy (STEM) images were collected using a probe-corrected Titan Themis 60-300 (Thermo Fisher Scientific) microscope. To modify the Z-contrast characteristics of the imaging mode, high-angle annular dark-field (HAADF) micrographs with a convergence angle of 23.8 mrad were acquired at 300 kV. The resulting collection angle ranges from 73 mrad to 200 mrad. Further energy-dispersive X-ray spectroscopy (EDS) analysis was conducted using Thermo Fisher Scientific's Super-X windowless EDS detector at an acceleration voltage of 300 kV. APT experiments were performed in a local electrode atom probe (LEAP 5000 XR) from Cameca Instruments Inc. and analysed with commercial AP Suite software (v6.1). A pulse frequency of 125 kHz, a pulse energy of 40 pJ and a temperature of 60 K was used. The detection rate was kept at a frequency of 1 ion per 100 pulses.

Mechanical response measurements

Room-temperature uniaxial tensile tests were performed using flat tensile specimens at an initial strain rate of 1×10^{-3} s^{-1}. The tensile specimens were machined along the rolling direction from the alloy sheets by electrical discharge machining. The specimens with a total length of 60 mm, a gauge length of 30 mm, a gauge width of 5 mm and a thickness of 2 mm were used to investigate the bulk tensile properties. Further, smaller tensile specimens with a total length of 20 mm, a gauge length of 10 mm, a gauge width of 2 mm and a thickness of 1 mm were used to measure the local strain evolution by the digital image correlation method. At least four specimens for each condition were tested to confirm reproducibility. Further, to clarify the relation between global strain–stress behaviour and microstructure evolution, we also conducted interrupted tensile tests on different global true strains (that is, 5%, 15% and 25%), and the microstructures in the middle part of the deformed regions were then characterized accordingly.

Magnetic response measurements

The magnetic response was evaluated using the Quantum Design Magnetic Property Measurement System (MPMS) equipped with a standard Vibrating Sample Magnetometry (VSM) option. Cuboid specimens of dimensions 3 mm × 3 mm × 1 mm (length × width × thickness) were used for the measurements. The hysteresis loops $M(H)$ were performed in an external magnetic field of ±800 kA m^{-1} at a magnetic field-sweeping rate of 1 kA m^{-1} at 10 K, 300 K, 500 K and 800 K, respectively. The temperature dependence of magnetization $M(T)$ analysis was carried out under an applied field of 40 kA m^{-1} from 10 K to 1,000 K with a temperature-sweeping rate of 10 K min^{-1}.

The magnetic domain patterns were characterized by a MOKE ZEISS microscope (Axio Imager.D2m). The domain wall movement was captured under an applied magnetic field of ±155 kA m^{-1}. Before the measurement, a background image was collected as a reference in the AC demagnetized state. The images acquired at different applied fields were enhanced by subtracting the background image using KerrLab software.

Physical response measurements

The electrical resistivity response was evaluated using the Quantum Design Physical Property Measurement System (PPMS) equipped with an Electrical Transport Option (ETO) option. Cuboid specimens of dimensions 6 mm × 2 mm × 1 mm (length × width × thickness) were used for the measurements. The resistivity ρ values are calculated by:

$$\rho = \frac{RA}{l}$$

in which R is the reported resistance, A is the cross-sectional area through which the current is passed and l is the voltage lead separation. The resistance value of each measurement is obtained by averaging those from 100 times of current passing. At least three specimens for each condition were tested.

Thermodynamic calculations

The equilibrium compositions of the fcc matrix and $L1_2$ particles in the $Fe_{32}Co_{28}Ni_{28}Ta_5Al_{l7}$ (at.%) alloy at 1,173 K were calculated using the Thermo-Calc software (v.2022a) equipped with the High Entropy Alloys database TCHEA v.4.2. The calculated equilibrium compositions for the fcc and $L1_2$ phases in the $Fe_{32}Co_{28}Ni_{28}Ta_5Al_7$ (at.%) alloy are $Fe_{36}Co_{31}Ni_{23}Ta_4Al_6$ and $Ni_{63}Ta_{13}Fe_6Co_3Al_{15}$ (at.%), respectively.

Estimation of particle size (edge length)

The size distribution is statistically analysed by applying a batch image-processing protocol with several 2D-projected ECC images of all the MCA samples at different annealed states (Extended Data Fig. 7). The average particle size (edge length) of the $L1_2$ particles is estimated by:

$$d = \sqrt{\frac{\sum S_i}{i}}$$

in which d is the average particle size, S_i is related to the area of each particle acquired from the 2D-projected ECC images by the batch image-processing protocol and i is the total particle number. The particle size of the M-MCA is also characterized by DF-TEM (Fig. 1d) and bright-field TEM (Extended Data Fig. 1). The TEM results fit well with the value acquired by ECC images.

Estimation of interfacial coherency stress

The coherency stress at the $L1_2$–fcc interface is determined by integrating the lattice misfit across the interface as:

$$\delta = S_{L1_2/fcc} \sum \delta_x$$

in which $S_{L1_2/fcc}$ is the $L1_2$–fcc interface area related to the average particle size (d), the volume fraction of the $L1_2$ particles (f) and the overall volume (V) as follows:

$$S_{L1_2/\text{fcc}} = \frac{Vf}{d^3} \cdot 6d^2 = \frac{6Vf}{d}$$

δ_x is the varying lattice misfit as a function of distance (x) from the $L1_2$–fcc interface determined by the following equation:

$$\delta_x = 2 \times \left[\frac{a_x^{L1_2} - a_x^{\text{fcc}}}{a_x^{L1_2} + a_x^{\text{fcc}}} \right]$$

$a_x^{L1_2}$ and a_x^{fcc} are the lattice parameters of the $L1_2$ and fcc phases at the interfacial region, respectively. Such values were calculated using the $L1_2$–fcc interfacial chemical compositions acquired from the APT datasets with Vegard's relation[51]:

$$a_x^{L1_2} = a_0^{L1_2} + \sum_i \Gamma_i^{L1_2} x_i^{L1_2}$$

$$a_x^{\text{fcc}} = a_0^{\text{fcc}} + \sum_i \Gamma_i^{\text{fcc}} x_i^{\text{fcc}}$$

in which $a_0^{L1_2}$ and a_0^{fcc} are the average lattice parameters for the $L1_2$ particles and the fcc matrix, respectively, derived from the Rietveld simulation based on the XRD measurements, as shown in Extended Data Table 1. $\Gamma_i^{L1_2}$ and Γ_i^{fcc} are the Vegard coefficients for the $L1_2$ and fcc phases, respectively, obtained from the ordered Ni_3Al phase and the disordered fcc phase in the Ni-base superalloys[52], as shown in Extended Data Table 2. Note that the above-calculated lattice misfit δ_l represents the theoretical unconstrained state. This can be related to the constrained misfit (ε) by elasticity theory as below[53]:

$$\varepsilon = \frac{3}{2}\delta_l$$

The estimated interfacial constrained misfit value is 1.09×10^6, 4.08×10^5 and 1.96×10^5 for the S-MCA, M-MCA and L-MCA, respectively. Therefore, the marked decrease in the interfacial coherency stress is expected to play an essential role in releasing the pinning effect on domain wall movement with particle coarsening for the MCAs with particle size below the domain wall width.

Estimation of dislocation density

The dislocation density (ρ) in the fcc matrix can be calculated through the Williamson–Smallman relationship as[54]:

$$\rho = \frac{2\sqrt{3}\,(\varepsilon_s^2)^{1/2}}{Db}$$

in which ε_s is microstrain, D is crystallite size acquired from the XRD profiles (Extended Data Table 1) and b is the Burgers vector (for fcc structure, $b = \sqrt{2}/2 \times a_{\text{fcc}}$)[55]. The dislocation density in the fcc matrix is thus estimated to be 1.50×10^{14} m^{-2}, 9.32×10^{13} m^{-2} and 5.38×10^{13} m^{-2} for the S-MCA, M-MCA and L-MCA, respectively. On the basis of the above estimation, the considerable improvement in the coercivity also derives from the decrease of dislocation density in the fcc matrix.

Estimation of particle shearing stress

On the basis of the experimental observation (Fig. 2c and Extended Data Fig. 2c), particle shearing is the primary deformation mechanism in the investigated MCAs. The strengthening contribution of particle shearing ($\Delta\tau$) is estimated according to[56]:

$$\Delta\tau_{\text{Shearing}} = \frac{F}{b \cdot 2\lambda}$$

in which 2λ is the mean spacing of the particles, $2\lambda \approx \sqrt{\frac{2}{f}} \cdot d$, d is the average particle size, f is the volume fraction of the particles shown in Extended Data Table 1 and F is the force exerted on the particles. The shearing strength is expressed as:

$$\Delta\tau_{\text{Shearing}} = k\sqrt{fd}$$

by using the relation $F \propto d^{3/2}$ and introducing constant k. The effect of particle strengthening of the M-MCA is then estimated to be two times larger than that of the S-MCA ($\Delta\tau_{\text{M-MCA}}/\Delta\tau_{\text{S-MCA}} = \frac{k\sqrt{f_{\text{M-MCA}}} \cdot r_{\text{M-MCA}}}{k\sqrt{f_{\text{S-MCA}}} \cdot r_{\text{S-MCA}}}$).

When considering the volume fraction of the particles to be constant, the mean spacing of the particles increases with increasing particle size. As a result, the force required for shearing particles increases until the Orowan mechanism is activated, that is, dislocations bowing the particles becomes easier than shearing. The critical mean spacing of the particles is determined by[56]:

$$\Delta\tau_{\text{Shearing}} = \frac{F}{b \cdot 2\lambda} = \Delta\tau_{\text{Orowan}} = \frac{Gb}{2\lambda}$$

$G = 84$ GPa is the adopted shear modulus[57]. Consequently, the critical mean spacing of the particles is calculated as 3,094.3 nm. However, in the current MCAs, the volume fraction of the $L1_2$ phase is not constant even after annealing at 1,173 K for 100 h. This is because the alloys have not yet reached the thermodynamical equilibrium state, as indicated by both thermodynamic calculations and APT analysis (Extended Data Fig. 5).

Estimation of magnetostatic energy

The magnetostatic energy (E_s) determines the coercive force that interacts between the paramagnetic particles (for M-MCA and L-MCA) and domain wall movement according to the formula[38]:

$$E_s = \frac{1}{2}\mu_0 \frac{1}{3} M_s^2 d^3$$

in which $\mu_0 = 4\pi \times 10^{-7}$ H m^{-1} is the permeability of vacuum, d is the average particle size and M_s is the saturation magnetization of the fcc matrix. For the M-MCA and L-MCA, in which the $L1_2$ phase is paramagnetic (Extended Data Fig. 4), the M_s of the fcc matrix is considered as the overall M_s of the alloy. The values of E_s markedly increase with increasing particle size, that is, it varies from 1.57×10^{-24} (M-MCA) to 3.65×10^{-23} (L-MCA). The notable increase in magnetostatic energy results in a strong magnetic pinning effect.

Estimation of domain wall width

Strong pinning arises and results in the deterioration of coercivity when the microstructure defects have a comparable dimension to the domain wall thickness (δ_w). As a result, the estimation of the δ_w to help understand the extremely low coercivity in the current work is given by[58,59]:

$$\delta_w = \pi(A_{\text{ex}}/K_1)^{1/2}$$

in which $A_{\text{ex}} = k_B T_c / 2a_0$ is the exchange stiffness, $k_B = 1.380649 \times 10^{-23}$ J K^{-1} is Boltzmann's constant and T_c and a_0 are the Curie temperature and lattice parameter of the fcc matrix, respectively (Extended Data Fig. 4d and Extended Data Table 1). K_1 is the first magnetocrystalline anisotropy constant. The value of K_1 (M-MCA) is taken from the Co–Fe system[60,61] based on the composition of the fcc matrix (Fig. 1f) as 10.4 kJ m^{-3} (Al and Ta are non-ferromagnetic elements that do not show any magnetic moment, the chemical composition of the fcc phase $Fe_{36}Co_{28}Ni_{26}Al_7Ta_3$ (at.%), in the M-MCA is thus considered as $Co_{31}(Fe+Ni)_{69}$ (at.%)). The domain wall thickness of the M-MCA is therefore estimated to be 112 nm. Similarly, the domain wall thicknesses of the S-MCA and L-MCA are calculated as 103 nm and 117 nm, respectively.

Data availability

Data and codes are available from the authors.

51. Mishima, Y. et al. Lattice parameters of Ni(γ), Ni₃Al(γ′) and Ni₃Ga(γ′) solid solutions with additions of transition and B-subgroup elements. *Acta Metall.* **33**, 1161–1169 (1985).
52. Okamoto, H. et al. in *ASM Handbook Volume 3: Alloy Phase Diagrams* (eds Okamoto, H., Schlesinger, M. E. & Mueller, E. M.) (ASM International, 1991).
53. Nembach, E. & Neite, G. Precipitation hardening of superalloys by ordered γ′-particles. *Prog. Mater. Sci.* **29**, 177–319 (1985).
54. Williamson, G. K. & Hall, W. H. X-ray line broadening from filed aluminium and wolfram. L'elargissement des raies de rayons x obtenues des limailles d'aluminium et de tungstene. Die verbreiterung der roentgeninterferenzlinien von aluminium- und wolframspaenen. *Acta Metall.* **1**, 22–31 (1953).
55. Callister, W. D. Jr. & Rethwisch, D. G. *Fundamentals of Materials Science and Engineering: An Integrated Approach* 5th edn (Wiley, 2018).
56. Rösler, J., Bäker, M. & Harders, H. *Mechanical Behaviour of Engineering Materials: Metals, Ceramics, Polymers, and Composites* (Springer, 2007).
57. Wu, Z. et al. Temperature dependence of the mechanical properties of equiatomic solid solution alloys with face-centered cubic crystal structures. *Acta Mater.* **81**, 428–441 (2014).
58. Néel, L. Bases d'une nouvelle théorie générale du champ coercitif. *Ann. Univ. Grenoble.* **22**, 299–343 (1946).
59. Pfeifer, F. & Radeloff, C. Soft magnetic Ni-Fe and Co-Fe alloys - some physical and metallurgical aspects. *J. Magn. Magn. Mater.* **19**, 190–207 (1980).
60. McKeehan, L. W. Ferromagnetic anisotropy in nickel-cobalt-iron crystals at various temperatures. *Phys. Rev.* **51**, 136–139 (1937).
61. Shin, J. W. Magnetic properties of iron-cobalt single crystals. *Phys. Rev.* **46**, 139–142 (1934).
62. Bradski, G. *Dr. Dobb's Journal: Software Tools for the Professional Programmer.* Vol. 25, pp 120–123 (2000).
63. Sundar, R. S. & Deevi, S. C. Soft magnetic FeCo alloys: alloy development, processing, and properties. *Int. Mater. Rev.* **50**, 157–192 (2005).
64. Zhou, K. X. et al. FeCoNiAlSi high entropy alloys with exceptional fundamental and application-oriented magnetism. *Intermetallics* **122**, 106801 (2020).
65. Zhao, C. et al. Effect of strong magnetic field on the microstructure and mechanical-magnetic properties of AlCoCrFeNi high-entropy alloy. *J. Alloys Compd.* **820**, 153407 (2020).
66. Wu, Z. et al. The AC soft magnetic properties of FeCoNiₓCuAl (1.0 ≤ x ≤ 1.75) high-entropy alloys. *Materials* **12**, 4222 (2019).

Competing interests The authors declare no competing interests.

Additional information
**Correspondence and** requests for materials should be addressed to Zhiming Li or Dierk Raabe.
Peer review information *Nature* thanks Todd Monson and the other, anonymous, reviewer(s) for their contribution to the peer review of this work.
Reprints and permissions information is available at http://www.nature.com/reprints.
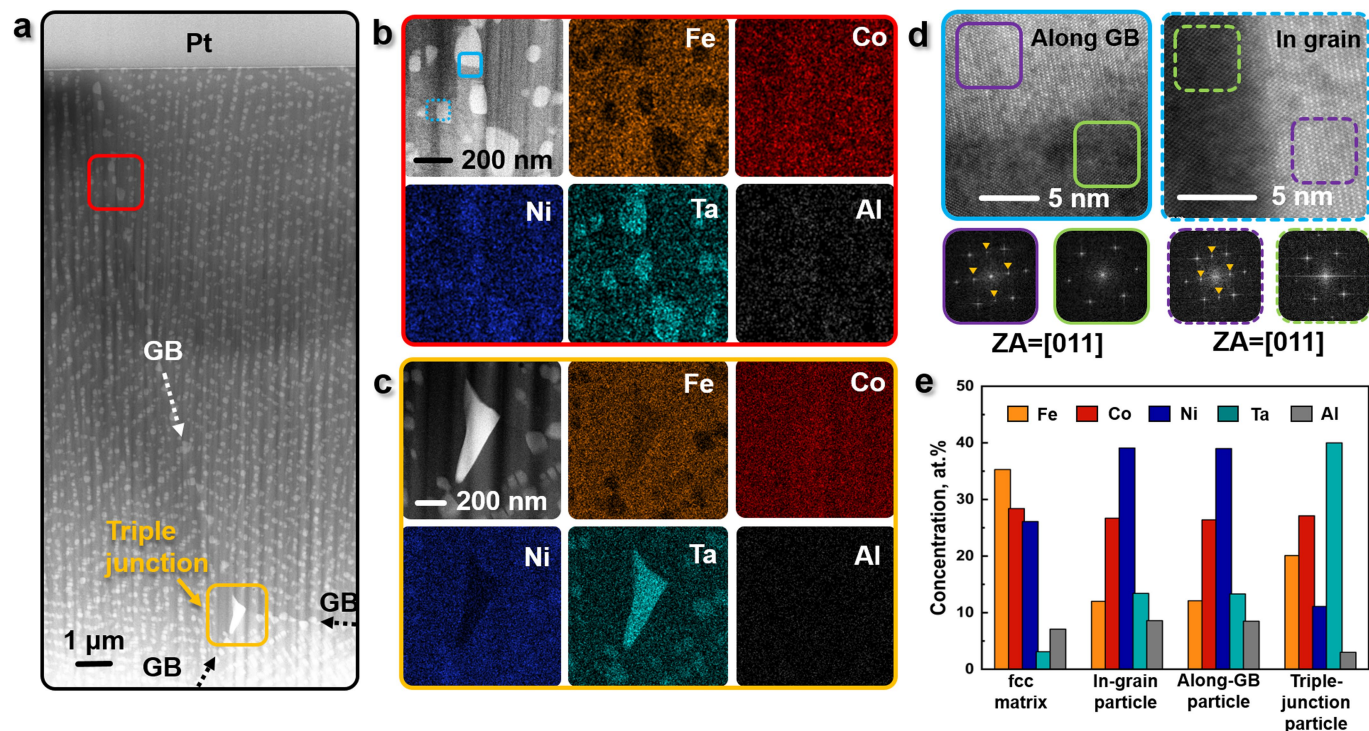
Extended Data Fig. 1 | STEM-HAADF micrographs and corresponding STEM-EDS analysis showing the structure and chemical composition of the particles with different morphologies. a, Overview of a STEM lamella showing the variation in particle morphology near the grain boundary. **b**, Enlarged view (red frame in **a**) showing particles inside the grains and along the GBs as well as their respective EDS elemental maps. **c**, Enlarged view (orange frame in **a**) illustrating a heterogeneous non-coherent particle at the triple junction of GBs and its EDS elemental maps. **d**, Atomically resolved HAADF-STEM micrographs and fast Fourier transforms of representative matrix and particle regions, indicating that the particles (ordered, bright) are coherent with the matrix (disordered, dark). The micrographs were obtained along the [011] zone axis. **e**, Comparison of the average chemical composition of different particles and the matrix determined by the EDS mapping. GB, grain boundary.
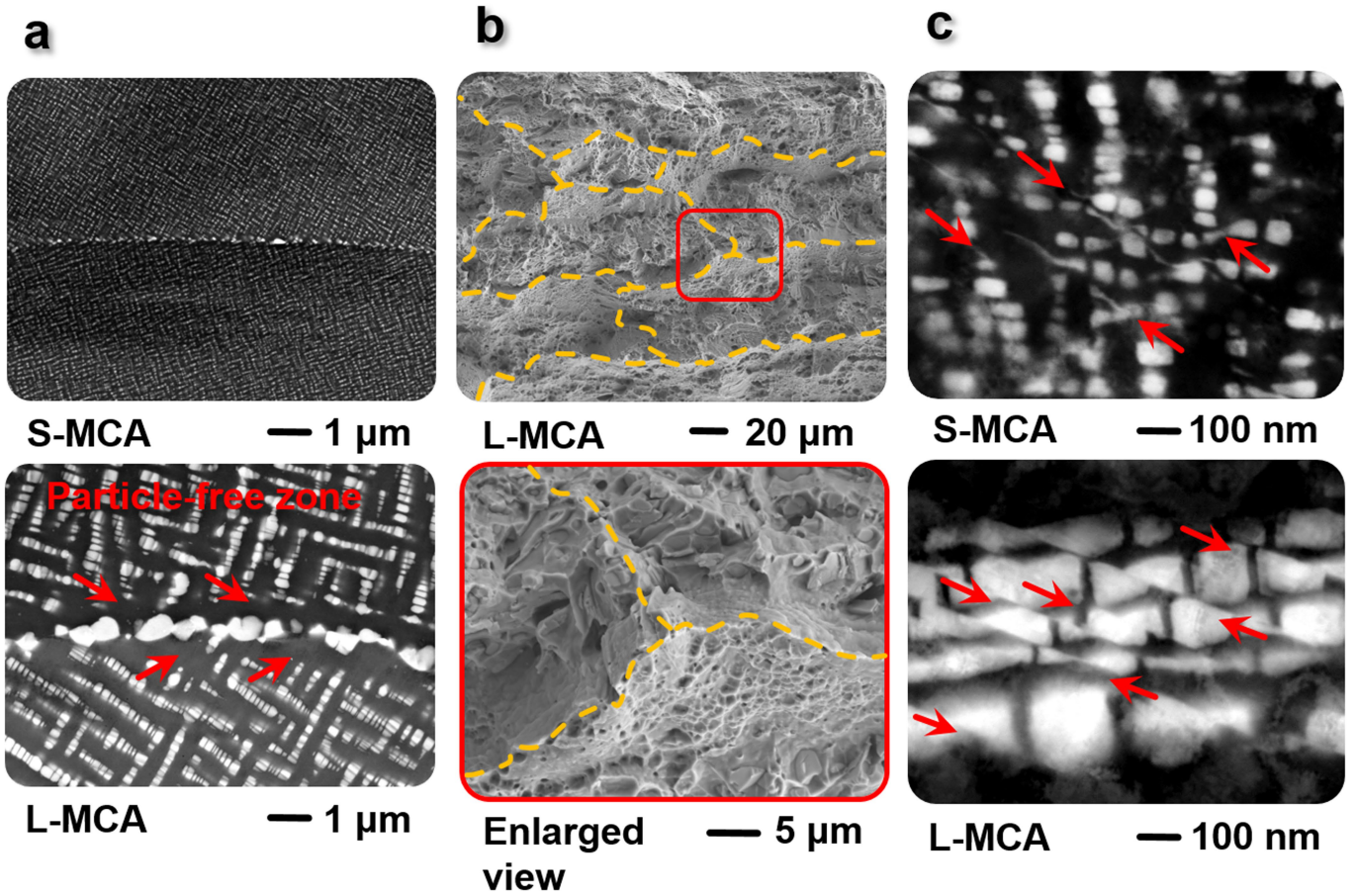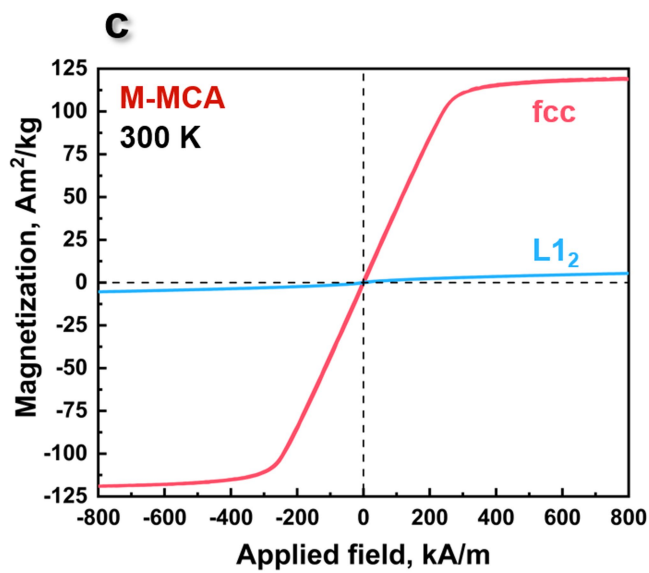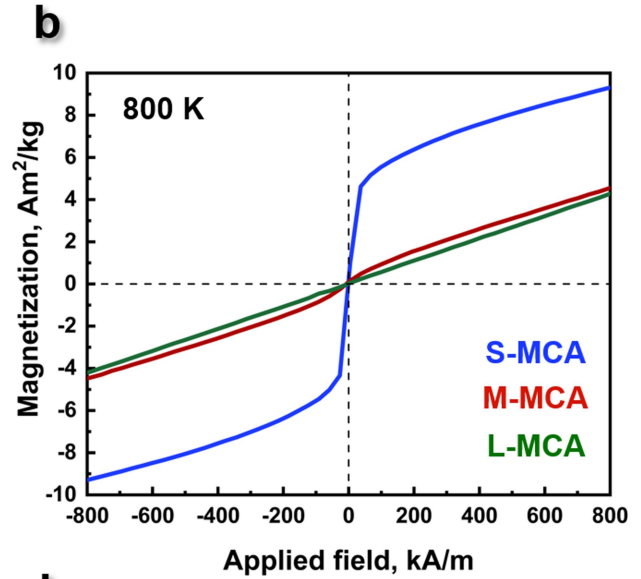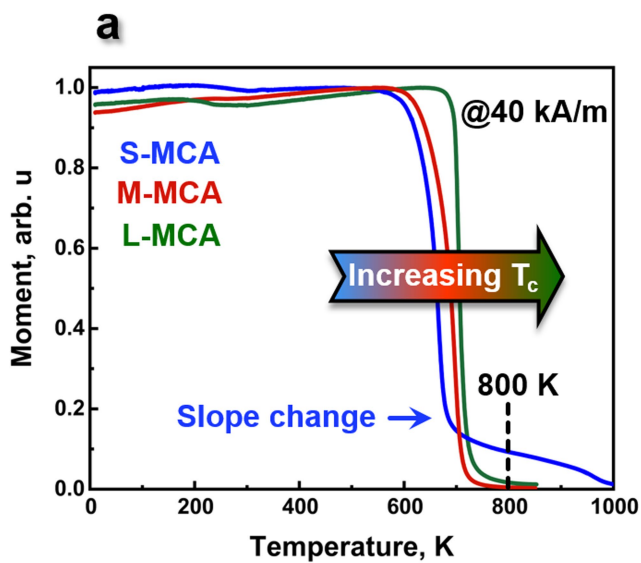
Extended Data Fig. 2 | Deformation mechanisms of the investigated MCAs.
a, ECC images of the S-MCA and L-MCA. The formation of the particle-free zone can be identified in the L-MCA. **b**, Fracture surface morphologies of the L-MCA. The enlarged view shows the presence of intergranular fracture at the triple junction of GBs with dimpled topology at one side of the grain facets. **c**, ECCI analysis showing the microbands and the shearing of the particles in the S-MCA and L-MCA.
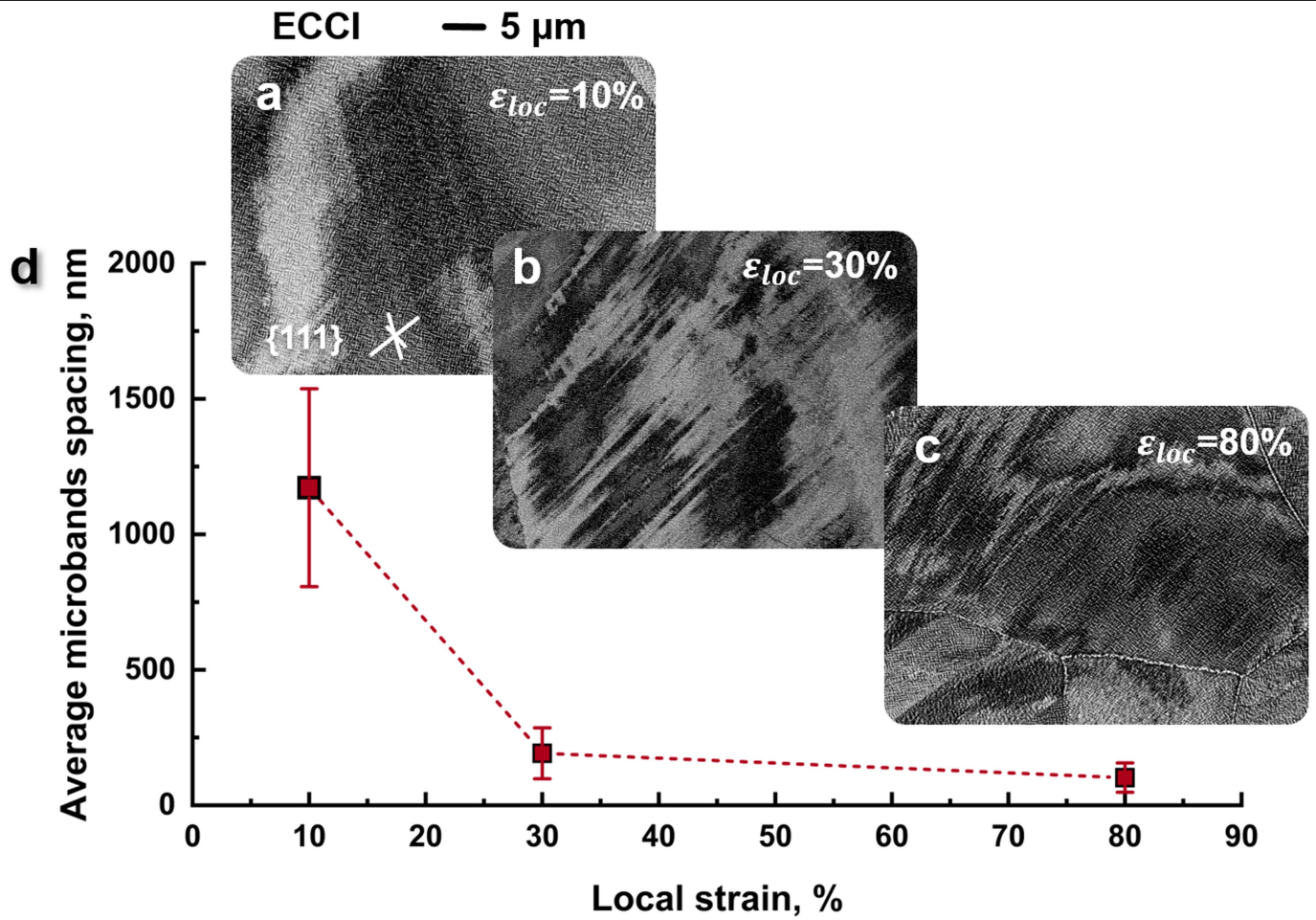
Extended Data Fig. 3 | Evolution of the microband refinement. a–c, ECCI analysis showing the evolution of microbands with increasing local strain (ε_{loc}) at 10%, 30% and 80%, respectively. **d**, Quantification of the decreases in average microband spacing with increasing local strain. The local strain has been estimated by the digital image correlation method.

a, M(T) curves measured in the temperature range 10–1,000 K under a magnetic field of 40 kA m⁻¹. **b**, M(H) loops of the MCAs measured at 800 K, confirming that the second phase in the S-MCA is ferromagnetic, with a T_c higher

Extended Data Fig. 4 | Magnetic behaviour of the MCAs in a wide temperature range. **a**, M(T) curves measured in the temperature range 10–1,000 K under a magnetic field of 40 kA m⁻¹. **b**, M(H) loops of the MCAs measured at 800 K, confirming that the second phase in the S-MCA is ferromagnetic, with a T_c higher than 800 K. The measuring temperature of 800 K was selected on the basis of the M(T) results as marked by a black dashed line in **a**. **c**, M(H) loops of the individual cast fcc and L1₂ phases in the M-MCA measured at 300 K. **d**, Temperature dependence of the M_s of the investigated MCAs.
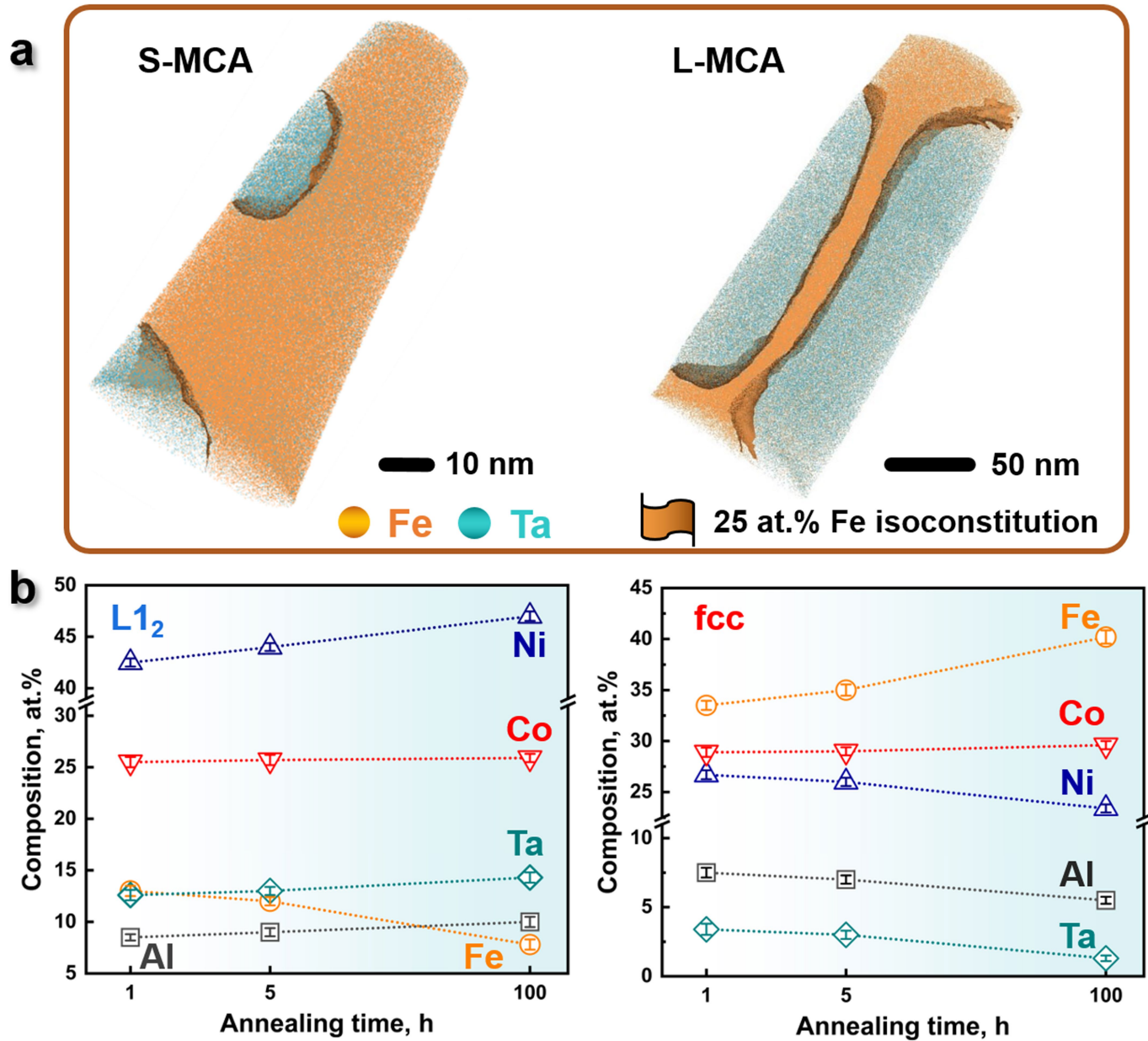
Extended Data Fig. 5 | Atom probe characterization showing the tomography and composition of the L1$_2$ particles and fcc matrix in the MCAs. a, APT datasets showing the reconstructed S-MCA and L-MCA containing L1$_2$ particles. **b**, Average chemical compositions of the fcc and L1$_2$ phases acquired from the APT subvolumes.
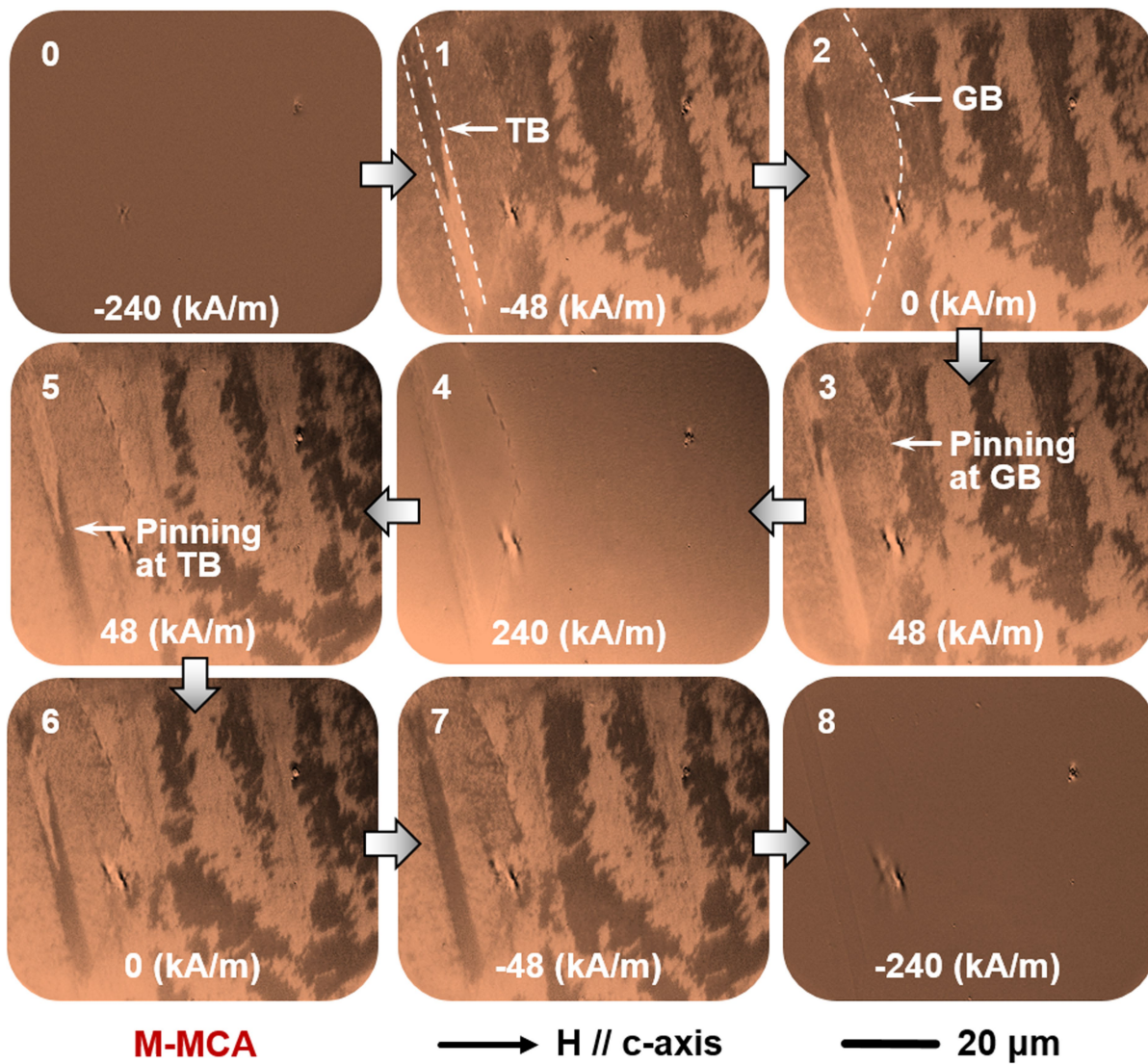
Extended Data Fig. 6 | MOKE microscopy observation showing the pinning of the magnetic domain wall during the magnetization process in the M-MCA.
GBs and TBs act as the pinning sites for domain wall movement. The applied magnetic field is horizontal to the viewing plane. GB, grain boundary; TB, twin boundary.
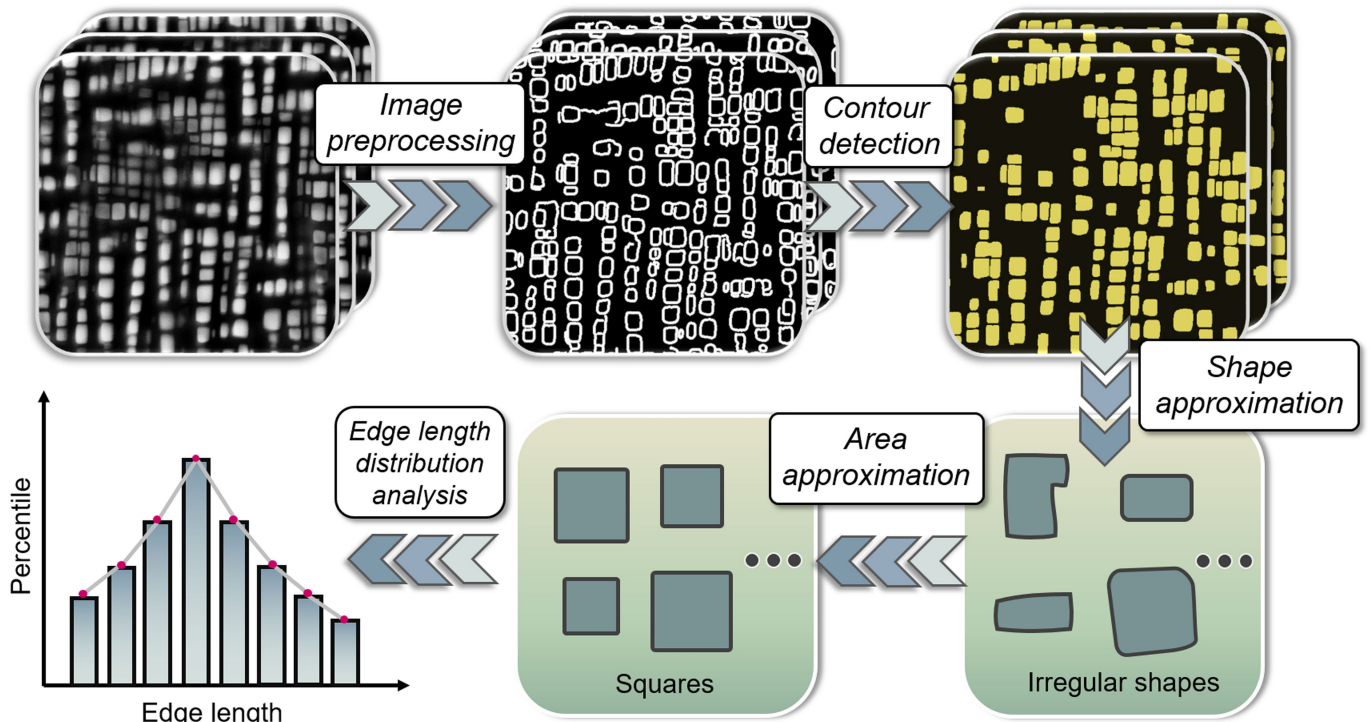
Extended Data Fig. 7 | Process for analysing the size distribution of the L1$_2$ particles by batch image-processing protocol. First, an edge detection algorithm was applied to the raw images to isolate particles from the matrix. Second, a contour detection algorithm was used to search for closed contours. Third, the particle shape was approximately evaluated and converted into a square shape. Finally, the size distribution of closed contours (particles) was computed. The algorithm was constructed using a Python[62]. For each sample, the particle size distribution was derived from more than 20 ECC images of different sample regions.
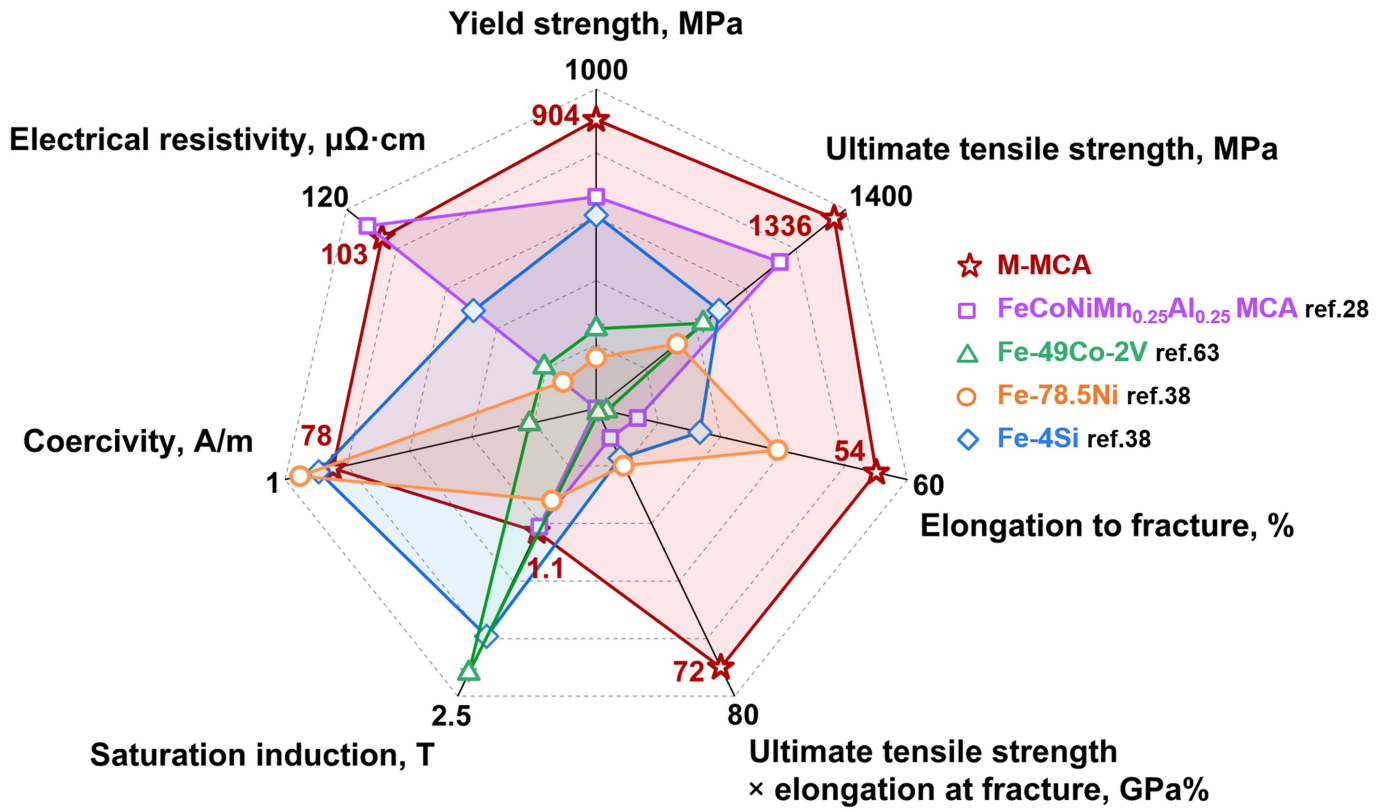
Extended Data Fig. 8 | Comparison of the mechanical and functional property spectra of the new MCAs and existing commercial SMMs. The representative commercial SMMs include silicon steel (Fe–4 wt.%Si (ref. [38])), a Fe–Ni alloy (Fe–78.5 wt.%Ni (ref. [38])) and a Fe–Co-based alloy (Fe–49 wt.%Co–2 wt.%V (ref. [63])).
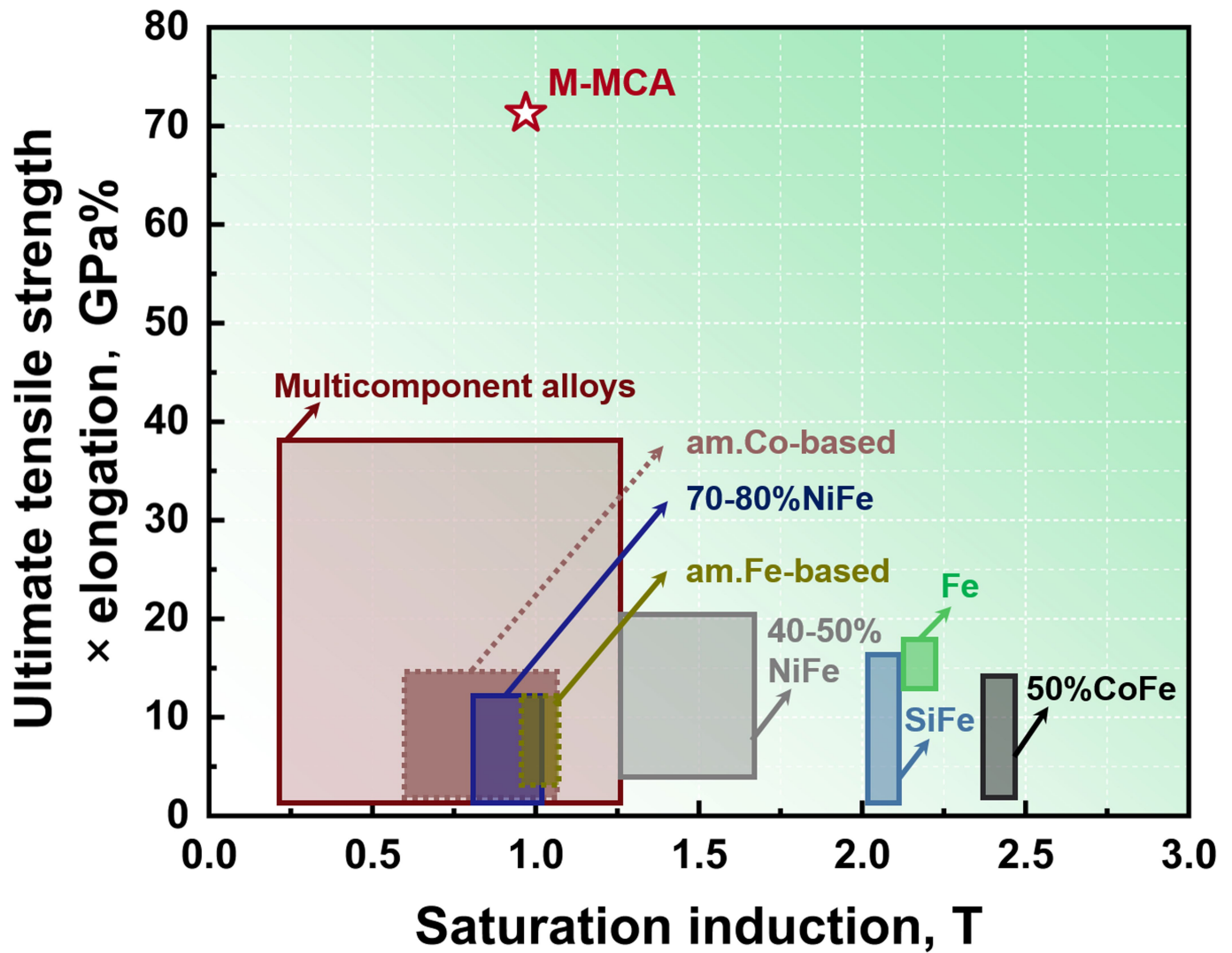
Extended Data Fig. 9 | Ashby map showing $\sigma_{UTS} \times T_E$ as a function of saturation induction (B_s). The investigated M-MCA is compared with a wide class of conventional SMMs, including Fe–Ni (refs. [24,25]), Fe–Si (ref. [38]), Fe–Co (refs. [39,40]), Fe (ref. [41]), amorphous alloys[42–45] and other MCAs[26–37]. The B_s is calculated using the equation $B_s = 4\pi M_s \rho_m/10,000$, in which $\rho_m = 8.6\ \mathrm{g\ cm^{-3}}$ is the mass density of the M-MCA.
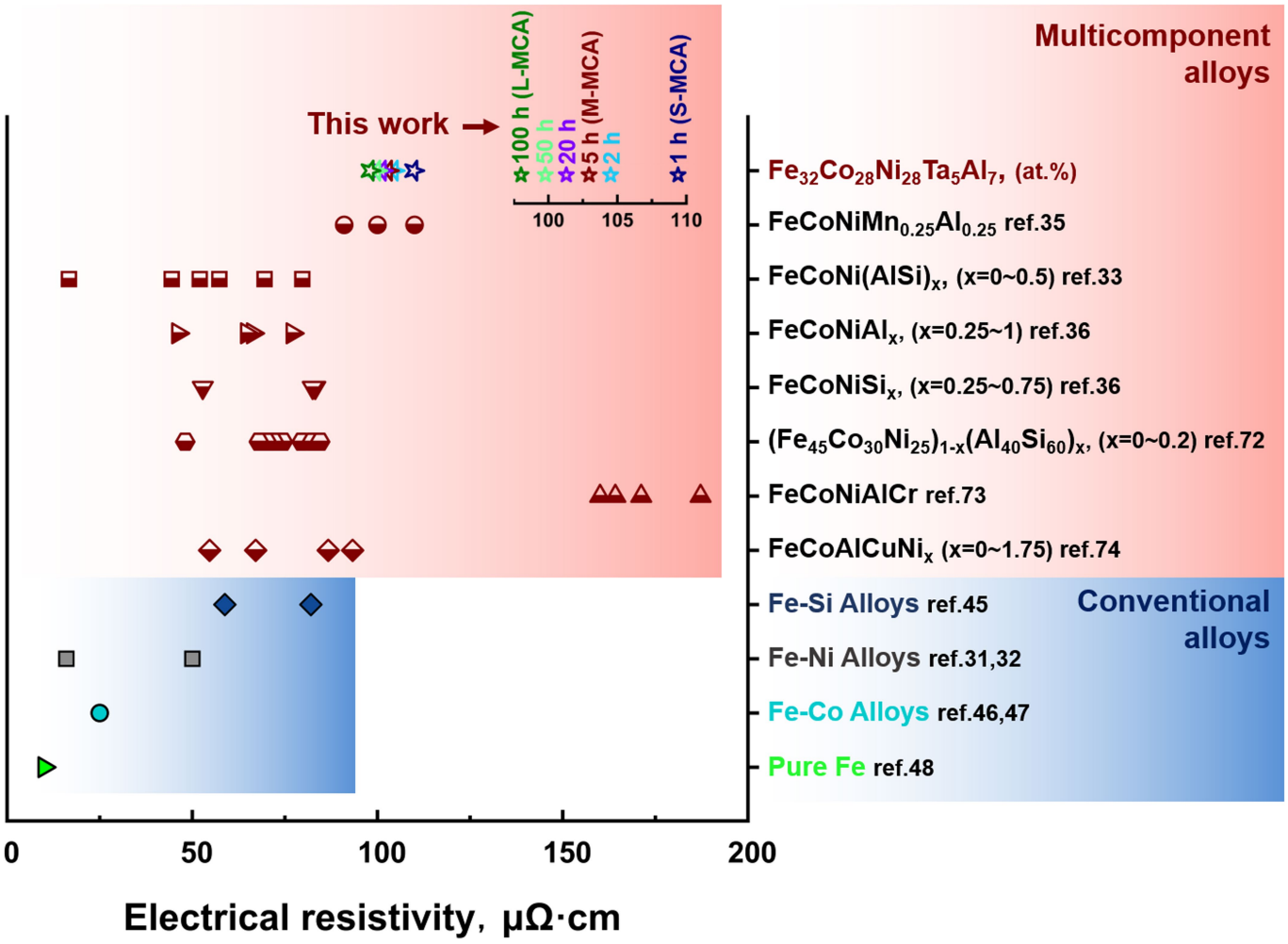
Extended Data Fig. 10 | Electrical resistivity of the $Fe_{32}Co_{28}Ni_{28}Ta_5Al_7$ (at.%) MCAs. The investigated MCAs are compared with a wide class of conventional SMMs, including pure iron, Fe–Ni (refs. [24,25]) alloys, Fe–Si (ref. [38]) alloys, Fe–Co (refs. [39,40]) alloys and other established MCAs[26,28,29,64–66]. The inset shows the evolution of electrical resistivity with increasing annealing time of the current MCAs.

Extended Data Table 1 | Structural parameters of the present MCAs

Alloys	S-MCA	M-MCA	L-MCA
a_0^{fcc} (Å)	3.6062 ± 0.0001	3.6050 ± 0.0001	3.6030 ± 0.0001
$a_0^{L1_2}$ (Å)	3.6223 ± 0.0001	3.6225 ± 0.0001	3.6228 ± 0.0001
Lattice misfit, δ_0 (%)	0.445	0.484	0.548
Volume fraction of the particle (%)	43.2 ± 0.5	55.2 ± 0.8	60.5 ± 1.0
Average particle size (nm)	23.9 ± 12.3	90.8 ± 35.8	255.5 ± 50.1
Average grain size (μm)	72.6 ± 16.9	85.3 ± 25.6	150.2 ± 50.4
Mean spacing of the particles (nm)	192.8 ± 74	65.5 ± 40.6	30.3 ± 17.3
Specific surface area (m^2/m^3)	$1.08{\times}10^8$	$3.65{\times}10^7$	$1.42{\times}10^7$
Specific surface area × integrated lattice misfit (%·m^2/m^3)	$1.09{\times}10^6$	$4.08{\times}10^5$	$1.96{\times}10^5$
Microstrain, ε_s	0.00084 ± 0.00002	0.00085 ± 0.00002	0.00087 ± 0.00002
Crystallite size, D (nm)	76 ± 4	124 ± 9	220 ± 40
Dislocation density (m^{-2})	$1.50{\times}10^{14}$	$9.32{\times}10^{13}$	$5.38{\times}10^{13}$

Extended Data Table 2 | Vegard coefficients in the disordered fcc phase and the ordered Ni₃Al phase taken from the Ni-base superalloys

Element (at%)	Fe	Ni	Co	Ta	Al
Γ_i^{γ} (Γ_i^{fcc})	0.123	0	0.02	0.725	0.179
$\Gamma_i^{Ni_3Al}$ ($\Gamma_i^{L1_2}$)	0.01	0	0	0.51	0